Investigation of flame topology and dynamics in a research rocket combustor

Untersuchung der Flammentopologie und -dynamik in einer Forschungsraketenbrennkammer

by

cand. ar. **John Luca Irtingkauf**

IRS-21-S-004

External Supervisor: M. Sc. Jan Martin
Responsible Professor: Prof. Dr. Stefan Schlechtriem

Institute of Space Systems

Faculty for Aerospace Engineering and Geodesy

University of Stuttgart

in cooperation with

Deutsches Zentrum für Luft- und Raumfahrt e.V.

(German Aerospace Center)

Lampoldhausen

May 2021

UNIVERSITÄT STUTTGART
INSTITUTE OF SPACE SYSTEMS

Pfaffenwaldring 29 · 70569 Stuttgart · Phone +49 (0) 711 685-62375 · Fax: +49 (0) 711 685-63596 · www.irs.uni-stuttgart.de

Master Thesis Work

of Mr. Luca Irtingkauf

Untersuchung der Flammentopologie- und -dynamik in einer Forschungsraketenbrennkammer

Investigation of flame topology and dynamics in a research rocket combustor

Motivation:

The Institute of Space Propulsion combines all activities of research on rocket engines and operation of rocket test stands. The research group for the investigation of combustion dynamics operates an experimental rocket combustion chamber fuelled with the cryogenic propellant combination of hydrogen and oxygen. The aim of the investigation conducted with this combustion chamber is to analyse the relationship between the acoustic field and the dynamic behaviour of the flame.

For this purpose, an optical access to the chamber is used to capture high-speed images of the high-pressure combustion. By evaluating the resulting data, the physical mechanisms of the flame dynamics shall be investigated.

Task description of the Master thesis work:

- In-depth familiarisation with the topic
- Adaption of the image processing tools
- Evaluation of the experimental data
- Investigation of the influence of injection conditions on the flame through analysis of optical recordings and comparison with sensor data
- Investigation of the interaction mechanisms through analysis of the optical images and comparison with dynamic pressure data
- Analysis of the combustion chamber acoustics
- Documentation of the test data and corresponding results

The thesis will be accomplished at the Institute of Space Propulsion, DLR Lampoldshausen

Supervisor: Jan Martin, M. Sc.

Starting date: 01.12.2020

Submission until: 31.05.2021

Prof. Dr. S. Schlechtriem
(Responsible Professor)

Acknowledgement of receipt:
I hereby confirm that I read and understood the task of the bachelor thesis, the juridical regulations as well as the study- and exam regulations.

Signature of the student

Declaration

I, ***Irtingkauf, Luca*** hereby certify that I have written this ***Master thesis*** independently with the support of the supervisor, and I did not use any resources apart from those specified. The thesis, or substantial components of it, has not been submitted as part of graded course work at this or any other educational institution.

I also declare that during the preparation of this thesis I have followed the appropriate regulations regarding copyright for the use of external content, according to the rules of good scientific and academic practice[1]. I have included unambiguous references for any external content (such as images, drawings, text passages etc.), and in cases for which approval is required for the use of this material, I have obtained the approval of the owner for the use of this content in my thesis. I am aware that I am responsible in the case of conscious negligence of these responsibilities.

Stuttgart, 31.05.2021 .....

Place, Date, Sign

I hereby agree that my ***Master thesis*** with the following title:

Investigation of flame topology and dynamics in a research rocket combustor

is archived and publicly available in the library of the Institute of Space Systems of the University of Stuttgart ***without blocking period*** and that the thesis is available on the website of the institute as well as in the online catalogue of the library of the University of Stuttgart. The latter means that bibliographic data of the thesis (title, author, year of publication, etc.) is permanently and worldwide available.

After finishing the work, I will, for this purpose, deliver a further copy of the thesis along with the examination copy, as well as a digital version.

I transfer the proprietary of these additional copies to the University of Stuttgart. I concede that the thesis and the results generated within the scope of this work can be used free of cost and of temporal and geographical restrictions for the purpose of research and teaching to the institute of Space Systems. If there exist utilization right agreements related to the thesis from the institute or third parties, then these agreements also apply for the results developed in the scope of this thesis.

Stuttgart, 31.05.2021 .....

Place, Date, Sign

[1] Stated in the DFG recommendations for „Assurance of Good Scientific Practice" or in the statute of the University of Stuttgart for „Ensuring the Integrity of Scientific Practice and the Handling of Misconduct in Science"

Abstract

This thesis presents novel experimental results on cryogenic jet flames formed by a coaxial injector at sub and supercritical pressures. The injector, fed with liquid oxygen and gaseous hydrogen, was placed in a research combustion chamber equipped with a quartz window, to allow for optical access. High-speed flame radiation imaging of OH* and blue wavelengths has been conducted in order to analyse the flame structure and the acoustic-flame interaction. A flame detection algorithm and intensity profiles were used to study the general shape of the flame. Dependencies of the flame topology on different injection parameters were identified. However, further work is required to quantify the influence of the individual parameters. Moreover, a simple modal analysis was conducted to propose likely sources of occurring oscillations. No self-excited instabilities were present in the recorded data and the overall behaviour appeared very stable. In addition, multi-variable dynamic mode decomposition was used to investigate two low amplitude oscillations. The first mode was traced back to be a slight excitation of the first longitudinal chamber mode. The source of the second mode remains uncertain, although it is suspected to be caused by a hydrodynamic free stream instability of the LOX core.

Kurzfassung

In dieser Arbeit werden neue experimentelle Ergebnisse zu kryogenen Jetflammen vorgestellt, die von einem Koaxialinjektor bei unter- und überkritischen Drücken erzeugt werden. Der mit flüssigem Sauerstoff und gasförmigem Wasserstoff gespeiste Injektor wurde in einer Forschungsraketenbrennkammer platziert, die mit einem Quarzfenster ausgestattet war, um einen optischen Zugang zu ermöglichen. Zur Analyse der Flammenstruktur und der Akustik-Flammen-Wechselwirkung wurden Hochgeschwindigkeitsaufnahmen der Flammenstrahlung in OH* und blauen Wellenlängen aufgezeichnet. Um die Form der Flamme zu untersuchen, wurde ein Algorithmus zur Flammenerkennung erstellt und eingesetzt, sowie Intensitätsprofile ermittelt und ausgewertet. Dabei wurden Abhängigkeiten der Flammentopologie von verschiedenen Einspritzparametern identifiziert. Um den konkreten Einfluss der einzelnen Parameter auf die Flammentopologie noch detaillierter quantifizieren zu können, werden jedoch noch weitere Experimente mit einer größeren Anzahl von Lastpunkten nötig sein. Eine einfache Modalanalyse wurde durchgeführt, um wahrscheinliche Quellen für auftretende Schwingungen zu identifizieren. Die Messdaten wiesen keine starken Verbrennungsinstabilitäten auf. Dennoch wurde eine multivariable Dynamic Mode Decomposition durchgeführt, um zwei Schwingungen mit geringen Amplituden zu untersuchen. Im Ergebnis konnte die erste untersuchte Mode auf eine leichte Anregung der ersten longitudinalen Eigenmode der Brennkammer zurückgeführt werden. Die Quelle der zweiten Mode blieb unklar; allerdings liegt die Vermutung nahe, dass sie durch eine hydrodynamische Freistrahlinstabilität des LOX-Kerns verursacht wird.

Contents

Nomenclature

Roman

Symbol	Description	Unit
A	Area	m^2
c	Speed of Sound	m/s
D	Diameter	m
J	Momentum Flux Ratio	-
L	Length	m
$\dot{m}$	Mass Flow Rate	kg/s
p	Pressure	bar
p'	Acoustic Pressure	bar
R	Radius	m
ROF	Oxidiser to Fuel Ratio	-
St	Strouhal Number	-
T	Temperature	K
u	Velocity	m/s
V	Volume	m^3
VR	Velocity Ratio	-

Greek

Symbol	Description	Unit
α	Spread Angle	$^\circ$
β	Bloom Angle	$^\circ$
η_{c^*}	Combustion Efficiency	-
ϕ	Phase	rad
ρ	Density	kg/m^3

Indices

Symbol	Description
$bulk$	Bulk, Total
cc	Combustion Chamber
$crit$	Critical Property
H_2	Hydrogen
O_2	Oxygen
WC	Window Cooling

Acronyms

BKN	Research Rocket Combustor 'Brennkammer N'
Blue	Blue Radiation
DLR	Deutsches Zentrum für Luft- und Raumfahrt e.V.
DMD	Dynamic Mode Decomposition
LP	Load Point
LPRE	Liquid-Propellant Rocket Engine
LOX	Liquid Oxygen
OH*	Hydroxyl Radical
PSD	Power Spectral Density
ROI	Region of Interest
UV	Ultraviolet

1. Introduction

Orbital infrastructure has become an integral part of the modern society. Whether it is the weather forecast in the morning, the navigation app on the drive to work or the evening news on TV, all rely on sizeable satellites in orbit. A prerequisite for any payload in orbit or in interplanetary space is a reliable launch vehicle. Today any launch vehicle with a substantial payload capacity is powered by liquid-propellant rocket engines (LPRE) and for the foreseeable future it is bound to stay that way [1]. One of the highest risks encountered in the development of LPREs are high-frequency combustion instabilities [2]. Even though the phenomenon is known almost as long as LPREs themselves [3], the underlying mechanisms are yet not completely understood [4]. Therefore, development of new engines is always linked to costly and laborious tests.

1.1. Scope

The aim of this work is to contribute to a deeper understanding of the phenomena, which may allow the development of improved methods for prevention and to reduce the need for extensive ground testing. For this purpose, an optical access to a research combustion chamber has been used to capture high-speed images of the combustion process. By evaluating the resulting data, the physical mechanisms of the flame dynamics will be investigated. Therefore, existing image processing tools shall be adapted to be used on the newly generated data. Consequently the influence of injection conditions on the flame will be investigated, through analysis of the optical recordings in comparison with sensor data. In another step the combustion chamber acoustics will be characterised, by comparing the measured data to analytical predictions of different modes. Finally a multi-variable dynamic mode decomposition (DMD) will be performed on the data to investigate the interaction mechanisms of pressure and flame intensity fluctuations at different frequencies.

1.2. Outline

This thesis is structured as follows: Chapter 2 contains a brief summary of the theoretical background surrounding the work. The experimental setup and techniques used to generate the data are expounded in chapter 3. Consequently the methods used to analyse the data are detailed in chapter 4. Chapter 5 holds a discussion of all the results extracted from the data. Finally, a conclusion is drawn and an outlook on future work is given in chapter 6.

2. Background

This chapter shall give an overview of the theoretical background surrounding the thesis at hand. In the first section LPRE are introduced, combustion instabilities are discussed in the second section, which is followed by summary of flame radiation in the third section. The last section contains a survey of flame topology correlations found in preceding investigations.

2.1. Liquid Propellant Rocket Engines

The principle of rockets using liquid fuel and oxidiser has been studied and developed since the early days of rocketry. The first rocket to reach edge of space, the first to reach orbit, and all rockets ever used to carry humans were propelled by LPREs [1]. Characterised by high performance, versatility and efficiency, they remain the propulsion system of choice for all medium- and heavy-lift launch vehicles to this day [5].

A LPRE generally consists of complex turbomachinery supplying a combustion chamber with an injector plate and an outlet nozzle. Due to the extreme conditions (cryogenic propellants and high pressure combustion) present in a bespoken engine, they are highly complex machines making up the largest single cost in rocket development [6].

2.1.1. Propellant Combinations

Numerous propellant combinations have been investigated and used in the past. The two relevant for the paper at hand shall be elaborated briefly in this subsection.

Liquid Oxygen-Hydrogen

The propellant combination of hydrogen (H_2) and liquid oxygen (LOX) delivers a very high theoretical performance and therefore has been, and still is, used in a variety of

rocket engines. As a result, the combustion is widely researched for the most part well understood [6]. Modern LOX/H_2 thrust chambers are often run at pressures above the critical pressure of both hydrogen and oxygen due to the relationship between chamber pressure and thrust output. At 20.4 K hydrogen has the lowest boiling point of all cryogenic propellants [2]. In addition to the extremely low density, this brings special requirements to the propellant tank infrastructure and turbomachinery, hence driving up the weight and cost.

Liquid Oxygen-Methane

In recent years a lot of research and development was conducted with methane (CH_4) as it promises a variety of advantages over hydrogen. The higher density and boiling temperature make it easier to handle, while the combustion process on the other hand is additionally complex [7].

2.1.2. Shear Coaxial Injectors

Injectors are designed to inject the propellants into the combustion chamber with preferably high combustion efficiency and stability. For LOX/H_2 fuelled engines, shear coaxial injectors are most commonly used, primarily because of their effective mixing properties for the LOX and gasous hydrogen (GH_2) stream [5]. In a shear coaxial injector, liquid oxygen is typically injected through a central tube, while fuel is injected through an annulus surrounding the LOX post. A schematic illustration of a shear coaxial injector can be found in Figure 1.

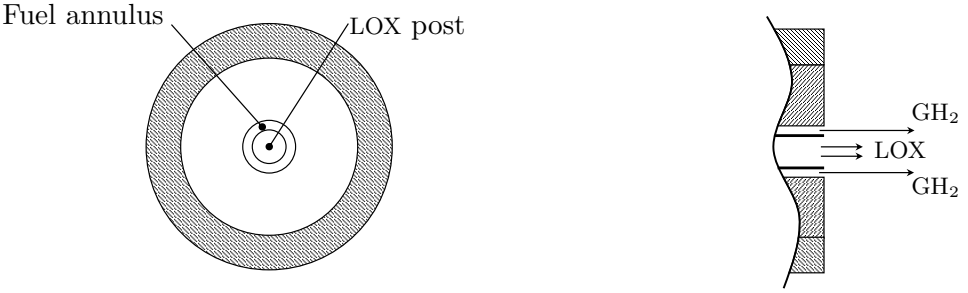

(a) Front View (b) Cross section

Figure 1.: Shear coaxial injector

The difference in injection velocity between the liquid core and the gaseous hydrogen jet from the injection annulus leads to an effective atomisation of the LOX jet and mixing of the propellants, hence achieving a high efficiency and a relatively stable combustion [8].

2.1.3. Supercritical Conditions

The state of a substance above the critical point is referred to as a 'supercritical fluid'. Instead of occurring in a distinguishable liquid or gaseous form, the behaviour of a supercritical substance can only be referred to as fluid. Small temperature variations near the critical point trigger significant changes in the fluid's specific volume and heat capacity. The critical pressure and temperature for oxygen and hydrogen can be found in Table 1.

Table 1.: Critical properties of hydrogen and oxygen [9]

Property	Hydrogen	Oxygen
Critical pressure (P_{crit})	12.8 bar	49.7 bar
Critical Temperature (T_{crit})	33.3 K	154.4 K

While in modern LOX/H_2 engines, hydrogen is injected at temperatures and pressures above its critical point, oxygen is commonly injected into the thrust chamber at supercritical pressure at a temperature below its critical temperature. As the LOX mixes with the already supercritical hydrogen, the extreme heat in the chamber rapidly raises the temperature above the critical point, causing the LOX to reach a fully supercritical state resulting in a fully supercritical combustion [8].

2.2. Combustion Instability

Fluctuations in the heat release and pressure are inevitable in any type of combustion. If the pressure oscillations exceed 5 % of the mean chamber pressure, they are referred to as combustion instabilities [2]. The frequencies at which they appear are determined by the geometry of the system, as they are often a result of excitation of the combustion chamber modes or resonance with the propellant feed system [8].

Due to the high energy release rates in thrust chambers, even marginal portions of the energy released by the combustion are sufficient to critically amplify the oscillations of the acoustic field, eventually leading to catastrophic failures [1]. Therefore, it is one of the most important issues faced by rocket designers and must be well understood for a successful LPRE design [8]. For rocket engines these instabilities are roughly categorised by their frequency as shown in Table 2:

Table 2.: Categories of combustion instability in rocket engines [2]

Instability	Frequency Range
Low frequency (LF)	$< 400\,\text{Hz}$
Intermediate frequency (IF)	$400 - 1000\,\text{Hz}$
High frequency (HF)	$> 1000\,\text{Hz}$

The different types of combustion instability shall be elaborated further in the following subsections.

Low Frequency Combustion Instability

As mentioned above, instabilities with a frequency below 400 Hz is commonly referred to as low frequency combustion instability or 'chugging'. They are commonly induced by periodic oscillations of the injector mass flow rates, coupling with pressure fluctuations in the thrust chamber. From the various kinds of instabilities, they are regarded as the easiest to control and handle from an engineering point of view [9].

Intermediate Frequency Combustion Instability

Intermediate instabilities or 'buzzing', occur when pressure perturbations in the combustion chamber are less than 5% of the mean and are not accompanied by considerable vibratory energy. Although buzzing can cause high-frequency instability, it is usually more bothersome and unpleasant than harmful. Coupling between the combustion process and flow in a section of the propellant feed system is a common occurrence [2].

High Frequency Combustion Instability

High frequency combustion instabilities also called acoustic instability or 'screeching' can appear, when unsteady heat release $\dot{q}'$, couples with the fluctuations in the pressure

field p', at the combustion chamber eigenmodes. In order to sustain the instability, a periodic release of thermal energy by the combustion process is necessary, which must be in phase with the acoustic pressure oscillation [9].

In 1878, RAYLEIGH observed, that to reinforce oscillations in acoustic pressure, they must be in-phase with oscillations in heat release [10]. While RAYLEIGH did not supply a mathematical formulation, PUTNAM and DENNIS introduced a formula of the *Rayleigh criterion* displayed by the integral below [11].

$$\int_0^{2\pi} \dot{q}' \cdot p' \, \mathrm{d}\varphi > 0 \tag{1}$$

If the phase shift between $\dot{q}'$ and p' is on the interval of $[-\frac{\pi}{2}, \frac{\pi}{2}]$, the integral over one period in Equation 1 yields a positive result, which is a necessary condition for the amplitudes of the oscillations to increase. If, on the other hand, the phase shift is on the intervals of $[-\pi, -\frac{\pi}{2}]$ or $[\frac{\pi}{2}, \pi]$ the criterion is not fulfilled and the oscillations are dampened. Physically this can be interpreted as the phase shift between $\dot{q}'$ and p' must not be greater than a quarter of a period, to maintain or excite the oscillations.

In LPRE, high-frequency instabilities commonly occur in three different modes: Longitudinal, transverse and combined. The longitudinal modes are standing waves extending from the injector face, along the axial chamber plain to the converging nozzle. The transverse modes form perpendicular to the chamber axis and can be further broken down into radial or tangential. The tangential modes can appear as standing waves as well as rotating waves [9]. Figure 2 shows a schematic illustration of the first longitudinal (1L), first tangential (1T) and first radial (1R) modes. Multiple superimposed longitudinal and transverse modes form complex three-dimensional oscillations, referred to as combined modes [8].
The tangential modes are regarded as the most damaging, as heat release rates can increase by a factor of up to ten [2]. The high power density in rocket combustion chambers entails, that LPREs are susceptible to instabilities as only a fraction of the energy present needs to be transferred into the acoustic field to rapidly reach high amplitudes of pressure oscillations. The enormous pressure peaks can lead to heat transfer rates multiple times higher than at stable operation. This can often melt the walls or the face plate and thereby cause a rupture of the chamber [2]. The exact reason why the pressure

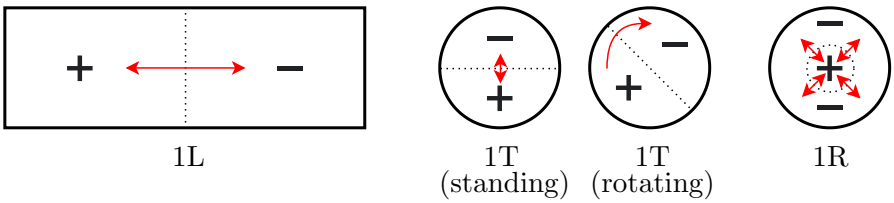

Figure 2.: First Order Longitudinal and transverse modes

oscillations lead to an increase in the heat flow to the wall is not yet fully understood. Therefore, extensive research has been conducted in all spacefaring nations to better understand and be able to predict these phenomena [12, 9].

2.3. Flame Radiation

Flames are visible to the human eye because the molecules in the combustion become excited, leading to the emission photons. This phenomenon is referred to as flame radiation. Two mechanisms are responsible for this effect: Thermal excitation and chemical excitation (chemiluminescence). For hydrogen - oxygen flames, chemiluminescence is typically dominant in comparably cold flames (below 2500 K), while thermal excitation increases above 2700 K [13]. Due to the hostile environments in rocket combustors, taking sophisticated measurements inside the thrust chamber can be very difficult. Thus, researchers in the United States, Russia, and Europe have conducted flame radiation measurements in model combustors to investigate flame-acoustic interaction [14].

The emitted spectrum of hydrogen-oxygen flames is rather simple, compared to hydrocarbon combustion, as only molecules containing hydrogen and oxygen atoms are present. In hydrogen flames, two types of radiation are dominant under rocket-combustion conditions: ultraviolet (UV) with a sharp peak at a wavelength of around 310 nm and blue radiation with a wide peak at a wavelength of around 440 nm. A typical radiation emission spectrum of a high pressure LOX/H_2 combustion can be found in Figure 3.
Both types are found to be strongly dependent on the ground-state hydroxyl radical concentration. Therefore, the emitted radiation is a good indicator of combustion intensity and location. The regions of emissivity of the two dominant radiations are found to be similar [14]. In the following two subsections, both types shall be expounded further.

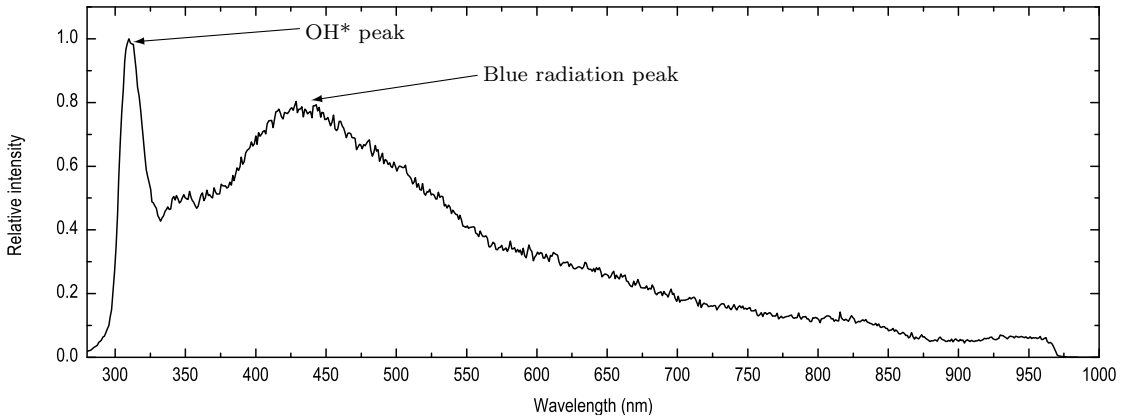

Figure 3.: Emission spectrum from a LOX/H_2 sub-scale combustor [8]

2.3.1. OH* Chemiluminescence

The most distinct radiation of flames in the UV spectrum is the radiation from the excited hydroxyl radical (OH*). Since its wavelength about 310 nm is so far in the UV spectrum that thermal background radiation [8] has no influence on the measured signal, it is often used as a flame marker [15, 16, 17]. As OH* is said to be in thermal equilibrium above 2700 K, chemiluminescence is the primary source of radiation from colder flames [13]. It is commonly agreed on, that hydroxyl radicals, which are not in thermal equilibrium during chemical reaction, form by the following reactions:

$$O + H \longrightarrow OH^* \tag{2}$$

$$O_2 + H \longrightarrow OH^* + H_2O \tag{3}$$

Lean to stoichiometric conditions have the highest radical concentration, and excited OH* have a brief life span before releasing a photon and returning to an unexcited state [8]. Chemiluminescence is therefore a good indicator of a flame's reaction zone. Unfortunately, the measurements get somewhat compromised from thermal excitation above 2700 K as temperatures in LPREs can reach temperatures of up to 3600 K [5]. In addition, the OH* radiation suffers from a high self-absorbtion at high pressures as Fiala et al. found [14].

Consequently, the integrated line of sight is mostly dominated by the flame surface closest to the optical access window. Moreover, an image intensifier is needed to transfer the UV radiation into the visible spectrum.

2.3.2. Blue Radiation

In addition to the well known UV radiation, hydrogen flames also show a broad continuous peak of high intensity at around 440 nm in the visible spectrum. The radiation is very weak at ambient conditions but increases with the chamber pressure, even surpassing the intensity of the sharp OH* emission at pressures above 60 bar [13]. The blue radiation, denoted as (Blue) in the following, emitted by hydrogen flames is the most visible to the human eye. The blue shimmering exhaust plume of the Vulcain Engine is a well-known example. The radiation is believed to stem from excited hydrogen peroxide (H_2O_2*) molecules, but physical proof for this hypothesis is still lacking [14]. The reaction forming H_2O_2* can be found in Equation 4.

$$OH + OH \longrightarrow H_2O_2* \tag{4}$$

According to Fiala et al., OH* and Blue radiations are highly affected by the concentration of ground-state OH* and increase at high temperatures. As a result, OH* and Blue radiations have the same structure. However, the Blue radiation suffers less from strong self-absorption allowing the flame dynamics to be analysed in a greater depth field then OH* [14]. Another benefit is that there is no need for UV sensitive optical equipment with Blue radiation.

2.4. Flame Topology of High Pressure Hydrogen-Oxygen Combustion

The flame topology, strictly speaking the 'flame geometry' of hydrogen-oxygen flames under rocket combustion conditions, has been the subject of numerous investigations [18, 19, 20]. Evidently the flame topology is dependent on a variety of parameters, such as chamber pressure (p_{cc}) and oxidiser-to-fuel mixture ratio (ROF), defined in Equation 5 below.

$$\text{ROF} = \frac{\dot{m}_{O_2}}{\dot{m}_{H_2}} = \frac{\text{Oxygen mass flow}}{\text{Hydrogen mass flow}} \tag{5}$$

However, a number of parameters are linked to specific flame behaviour. For instance it is widely accepted that the inner-to-outer-propellant injection velocity ratio (VR), defined by Equation 6, greatly influences the atomisation and consequently the mixing characteristics in coaxial injection [21]. Velocity ratios of modern LOX/H_2 engines usually span from $10 - 20$ [5]. By governing atomisation and mixing of the propellant, the VR also greatly influences the combustion efficiency η_{c^*} [22]. Another important parameter that characterises the injection, is the inner-to-outer-propellant injection momentum flux ratio (J), defined by Equation 7. The momentum flux ratio indicates the shear forces between the injected propellants [8].

$$\text{VR} = \frac{u_{H_2}}{u_{O_2}} = \frac{\text{Hydrogen injection velocity}}{\text{Oxygen injection velocity}} \tag{6}$$

$$J = \frac{\rho_{H_2} \cdot u_{H_2}^2}{\rho_{O_2} \cdot u_{O_2}^2} = \frac{\text{Hydrogen injection momentum flux}}{\text{Oxygen injection momentum flux}} \tag{7}$$

Hydrogen-oxygen flames are generally attached to the LOX post at steady state operating conditions, due to their high flame speed [22]. After following the liquid oxygen jet right after injection, the flame expands when the liquid jet begins to disintegrate. This characteristic flame expansion is particularly dependent on the shear forces between the injected propellants, leading to the LOX core break-up. JUNIPER et al. observed, that an increase in momentum flux ratio leads to both a smaller spreading angle and a more constricted flame [19]. In addition to, that flame expansion is reduced at high pressure and is also less dependent on the momentum flux ration, compared with low pressure. In contrast KENDRICK et al. observed, that an increase of the J-number leads to a faster breakup of the liquid jet, improved primary atomisation and hence an earlier widening of the flame [23].

In the past, investigations of flame topology have been more or less limited to small regions of the combustion chamber, as optical access was only possible with relatively small windows compared to the chamber dimensions. Nevertheless attempts have been made to analyse the topology of a flame on full length. In a study conducted by SUSLOV

et al. an optical access window was placed in different positions on the Deutsches Zentrum für Luft- und Raumfahrt e.V. (DLR) research thrust chamber 'C'. The same injection conditions were repeated and the recordings were later stitched together. It was found, that for a range of momentum flux ratios between 1.3 and 4.2, the LOX core length collapses with rising J [18].

2.4.1. Influence of Reduced Pressure

A common parameter to describe the thermodynamic state of a fluid is the reduced pressure (p_r) as defined by Equation 8.

$$p_r = \frac{p_{cc}}{p_{crit}} \tag{8}$$

The reduced pressure of the injected propellants has a significant influence on the flow field evolution and the entire combustion process in a LPRE thrust chamber [22]. Since the critical pressure of hydrogen is relatively low, compared to the pressures present in rocket combustors, subcritical hydrogen is not considered here. Shadowgraphy imagery of substitute fluids with a subcritical and supercritical liquid nitrogen (LN_2) jet and a gaseous helium (He) surrounding can be found in Figures 4a and 4b, respectively. As can be seen in Figure 4, the LN_2 core break-up behaviour varies considerably depending on the p_r of nitrogen. In the subcritical domain the liquid core atomises and forms droplets, which spray into the surrounding hydrogen stream. In the supercritical domain on the other hand, the liquid core mixes with the hydrogen without forming droplets.

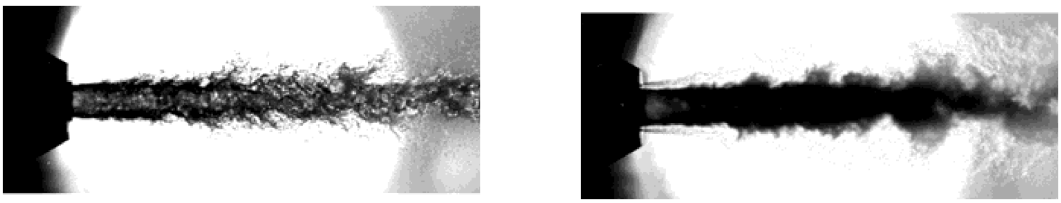

(a) Subcritical (p_r=0.3) (b) Supercritical (p_r=1.77)

Figure 4.: Shadowgraphy of coaxial LN_2/He injection [20]

According SMITH et al., there is a noticeable difference in thrust chamber activity at pressures below, close, and above the critical pressure of oxygen leading to a prominent variation in combustion efficiency [22].

3. Methodology

In this chapter, the methodology used to acquire the evaluated data will be elaborated. The first section holds an overview of the the experimental set-up and the test runs carried out. In the following section the utilised diagnostics techniques are expounded. The last section of this chapter contains an explanation of all the methods used to process the raw data to acquire the prospected results presented in chapter 5.

3.1. Test Operations

This section consists of a brief summary of the test facility P8 at DLR Institute of Space Propulsion near Lampoldshausen, the DLR research rocket combustor 'Brennkammer N' (BKN) and the test runs carried out.

3.1.1. Test Facility P8

The hot firing test runs of BKN, analysed in this thesis, were conducted at the European Research and Technology Test Facility P8. The test facility was built in 1995 as part of a European cooperation between multiple partners, to test rocket engines using various propellants. The infrastructure on site provides liquid and gaseous hydrogen, oxygen and methane, amongst other fluids. It allows precise and fast mass flow control and operating pressures up to a maximum of 360 bar. It therefore allows for rocket combustor tests at realistic operating conditions [24]. A photograph of the test facility P8 during a test run is shown in Figure 5.

3.1.2. Combustion Chamber 'N'

The combustion chamber 'N' was specifically developed and constructed to provide optical access into a combustion chamber with a main-stage engine-scaled injector at sub

Figure 5.: Test Facility P8 during a Test Run

and supercritical conditions. BKN consists of an injector head, a cylindrical combustion chamber and an exhaust nozzle. The injection plane, the ignition system and the exhaust nozzle are exchangeable, providing a 'test platform' for different components. The chamber has a length of 362 mm from the injection plane to the nozzle throat and a diameter of 50 mm. To allow for optical access, the cylindrical thrust chamber has two access windows facing opposite sites. Quartz glass windows can be installed on either one or both sides, to enable capture and back lighting of the inside, respectively. These optical access windows can also be interchanged with metal dummy windows, equipped with sensors, in case optical access or back lighting is not needed. To avoid disrupting the symmetry of the combustor's flow field, the windows have a curved inner surface. A rendering of the chamber with the quartz glass window installed can be found in Figure 6a.

With a length of 254 mm and a height of 38 mm the windows span along more than two thirds of the chamber length. This allows for novel investigations as no other high-pressure combustor, in comparable dimensions, has ever been fitted with a window stretching a similar length.

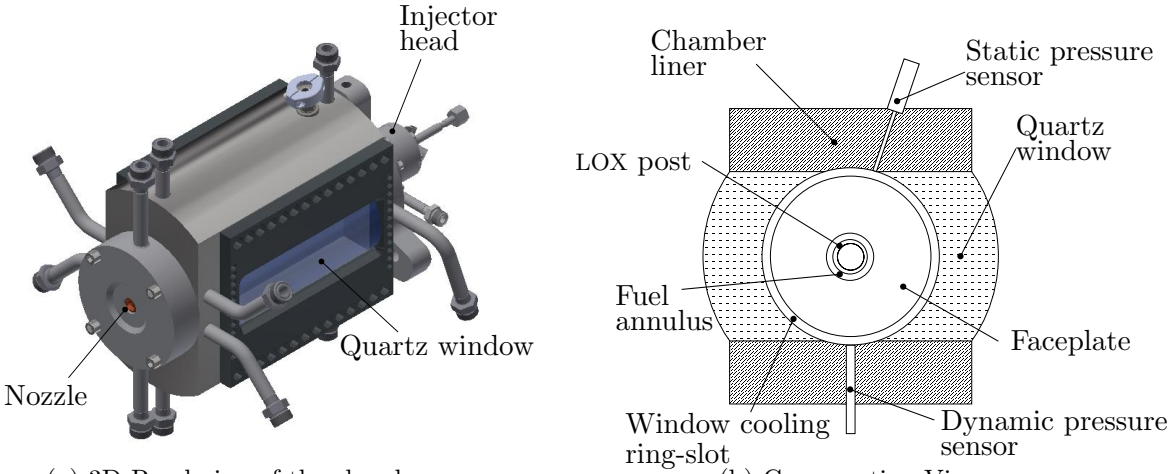

(a) 3D Rendering of the chamber

(b) Cross section View

Figure 6.: DLR subscale combustion chamber BKN

Configuration

For the test runs evaluated in this thesis, a dummy window manufactured of stainless steel was placed on one side, while the other one was equipped with a quartz glass optical access window. A schematic cross section of the installed window configuration is illustrated in figure 6b.

A single, centrally positioned, recessed shear coaxial injector was installed on the injector head. The injector is a hybrid, as the design allows it to be used with LOX/H_2 as well as LOX/CH_4. Since the density of methane is considerably higher than the density of hydrogen, the fuel annulus is designed rather small compared to typical LOX/H_2 injectors. This leads to very high H_2 injection velocities, somewhat compromising the comparability to other experiments. A drawing of the injector is displayed in figure 7, with the recess indicated in red.

The reaction inside a high pressure LOX/H_2 combustor can reach temperatures up to 3600 K [5]. To keep the quartz glass below its maximum operating temperature of 1600 K, a H_2 cooling film was injected through a ring slot, at the outer diameter of the chamber and at ambient temperature. The ring slot is also depicted in the Figure 6b The hydrogen cooling film, referred to as window cooling (WC), also prevented contact of the combustion products with the window surface.

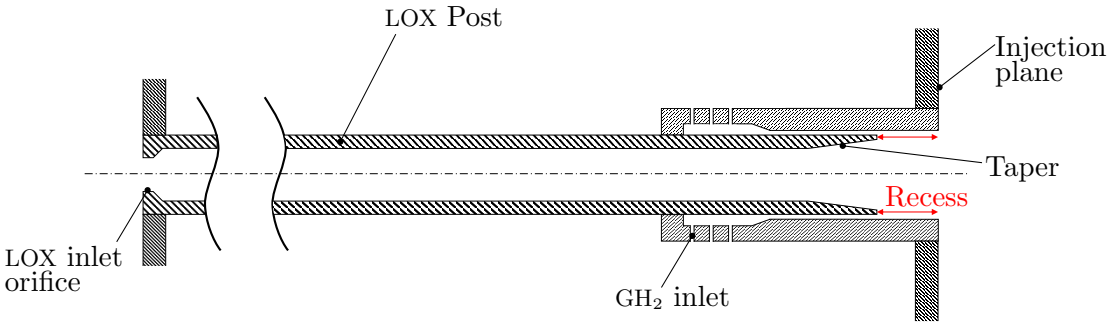

Figure 7.: Injection Element

Thereby the accumulation of condensed water on the inner surface was inhibited, maintaining a clear optical path. The film injection velocity has been held as close to the velocity of the hot gas main flow as possible, at all operating conditions to improve cooling efficiency. This also replicates the conditions in a multi-injector combustion chamber with co-flow.

3.1.3. Test Sequences and Achieved Operating Conditions

Three test runs were conducted with the configuration detailed in section 3.1.2. The corresponding test sequences are shown in figure 8, with the camera recording times indicated in grey.

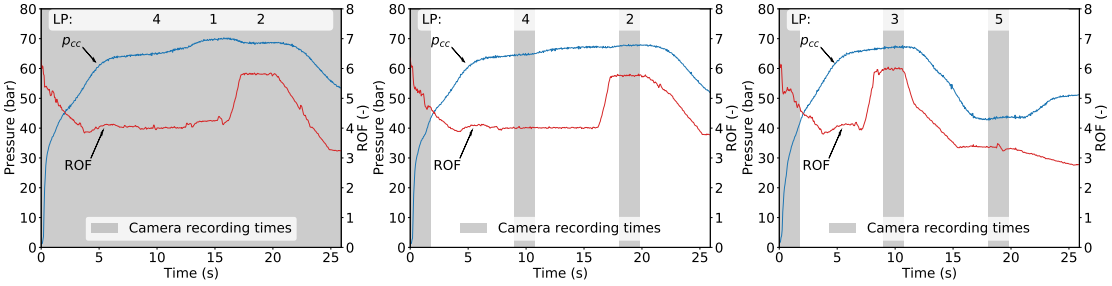

(a) 07run3 (b) 07run5 (c) 07run7

Figure 8.: Test Sequences

In the first two test runs (07run3 and 07run5), almost the identical test sequence was used. As indicated in figures 8a and 8b, they mostly differed in camera recording time. While the cameras recorded the whole test run 07run3, in 07run5 only the run up and two

stationary load points (LP)s were optically documented. For the last test run (07run7), two different load points were realised with the cameras recording again during run up and two stationary operation points, similar to 07run5. The recording details are further specified in section 3.2.1.

Load Points

A load point is defined by mostly static combustion chamber pressure p_{cc} and injection conditions, such as propellant massflows ($\dot{m}_{O_2}, \dot{m}_{H_2}, \dot{m}_{WC}$) and fluid temperatures (T_{O_2}, T_{H_2}, T_{WC}). In the work at hand five LPs are investigated. Their specifications can be found in Table 3, with the data points being calculated mean values over a sample period of 1.8 s. The ROF (indicated as ROF_{inj} in Table 3) was varied by changing the H_2 massflow. To examine the influence of the window cooling massflow, a total oxygen (O_2) to H_2 ratio, denoted ROF_{bulk} was defined by equation 9.

$$\mathrm{ROF}_{bulk} = \frac{\dot{m}_{O_2}}{\dot{m}_{H_2} + \dot{m}_{WC}} \tag{9}$$

Modern upper stage H_2/O_2 engines typically operate at chamber pressures well above 50 bar and oxidiser to fuel ratios of 4.5-6 [2]. To depict the flame behaviour of industrial engines in operation, similar operating conditions were realised.

As the test runs investigated in this thesis were the first hot firing runs to be conducted with BKN, the dynamic behaviour of the chamber was essentially unknown. However, possible combustion instabilities resulting from the dynamic behaviour are of particular interest. Previous investigations of different model combustors found that the coupling of heat release and acoustic perturbations, resulting in combustion instabilities is particularly dependent on ROF and p_{cc} [25, 4, 17]. Therefore, four load points at high pressure were realised: Two of them with a high ROF (2,3) and two of them with low ROF (1,4). At all four high pressure LPs, both propellants were injected in a supercritical state. Additionally, a fifth load point (5) with an even lower ROF and p_{cc} than 1 and 4 and therefore subcritical oxygen injection was achieved.

Table 3.: Operating Conditions

Load point		1	2	3	4	5	Max. uncertainty
p_{cc}	bar	69.9	68.1	67.1	64.9	43.4	±1.1%
ROF[a]	-	4.3	5.8	6.0	4.0	3.3	±5%
ROF_{bulk}[a]	-	1.1	1.2	1.2	1.2	1.4	±5%
$\dot{m}_{O_2}$	g/s	349	347	347	329	234	±3%
$\dot{m}_{H_2}$	g/s	82	60	58	82	70	±3%
$\dot{m}_{WC}$	g/s	228	229	228	200	100	±3%
p_{O_2}	bar	102.6	100.7	100.6	94.4	58.8	±1.1%
p_{H_2}	bar	110.8	91.4	92.0	107.8	92.0	±1.3%
p_{WC}	bar	162.6	163.7	161.8	141.6	72.1	±1.3%
T_{O_2}	K	112	113	115	113	115	±3.5 K
T_{H_2}	K	169	168	163	167	162	±3.5 K
T_{WC}	K	303	304	299	299	306	±2.0 K
u_{O_2}[a]	m/s	11	11	11	10	7	
u_{H_2}[a]	m/s	711	530	505	754	916	
u_{WC}[a]	m/s	277	286	284	257	194	
VR[a]	-	66.5	49.6	46.8	74.3	124.6	
J[a]	-	40.3	22.1	20.2	47.8	96.2	

[a] Calculated parameter.

3.2. Diagnostics and Data Acquisition

The measurement techniques used to acquire the data shall be elaborated in the following two subsections.

3.2.1. Optical Diagnostics

Optical measurements were taken by two high-speed camera systems that recorded synchronously. To capture OH* emission as well as Blue radiation, the optical axis was divided by a dichroic mirror to allow an equal field of view for both camera systems. The imaging setup is depicted in a simplified schematic form in Figure 9.

A Photron Fastcam SA-Z and a camera lens with 50 mm focal length were used to perform Blue radiation imaging. A blue filter was placed in front of the SA-Z camera lens, allowing only light with a wavelength of 436 nm ± 5 nm to pass through. To capture the OH* emission, a Photron Fastcam SA-X2 with an image intensifier and an

UV sensitive F-mount lens with 105 mm focal length were used. Additionally, an UV band-pass filter with a central wavelength of 310 nm was placed in front of the lens.

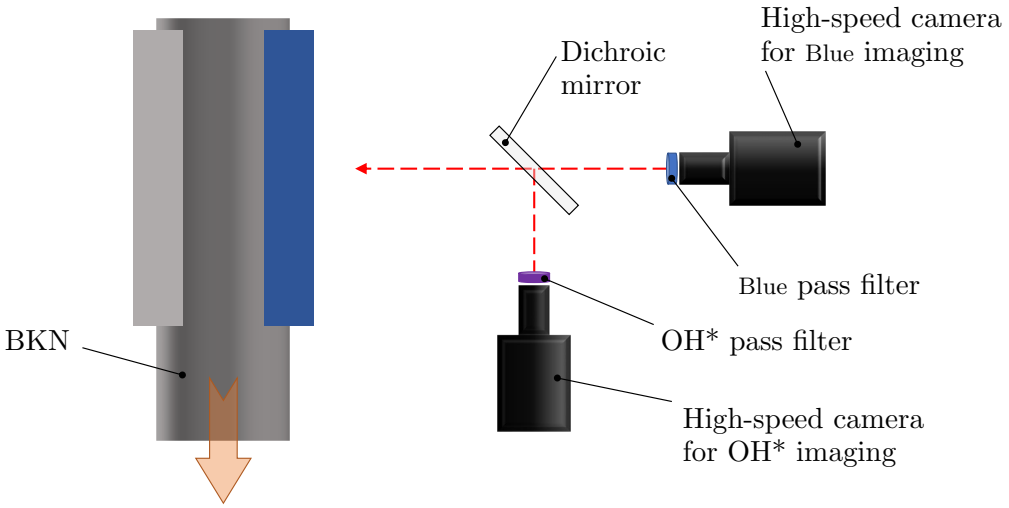

Figure 9.: Principal scheme of the optical diagnostic setup

Different frame-rates were selected for the different test runs to enable static as well as dynamic analysis. Test run 07run3 was captured with both cameras recording with 3,000 fps to allow investigation of the flame topology for the whole test run. During the latter two test runs 07run5 and 07run7, both cameras were set to record at 20,000 fps. As the RAM capacity of the Photron Fastcams is limited, recording of the whole test run at full resolution was not possible with the given frame-rate. Consequently, the recording time was set to the run up and two steady state LPs for both test runs, as indicated in Figure 8. The high frame rates hereby allow for the investigation of high frequency flame dynamics.

3.2.2. Measurement Technique

Thermocouples, static pressure sensors, and dynamic pressure sensors were installed into the injection manifolds, to record the injection conditions for LOX , cold GH_2, and window cooling. Numerous sensors of the same kinds were also present in the combustion chamber itself. The investigation at hand is primarily based on the sensors mounted in the injection manifolds and the first static pressure sensor, positioned 4.5 mm into

the chamber recording at 100 Hz. Furthermore, six unsteady pressure sensors inside the chamber, which were flush mounted downstream of the face plate at distances of 34.5 mm, 84.5 mm, 94.5 mm, 134.5 mm, 164.5 mm, and 234.5 mm, were used to study the dynamic behaviour of the chamber pressure. The signals of the dynamic pressure sensors were measured at a rate of 100 kHz and were set to a $\pm$ 30 bar measurement range.

4. Data Analysis

The methods used to analyse the collected data are expounded in the following three subsections.

4.1. Image Pre Processing

Optical distortion is prominent in all imagery taken during the test runs. The distortion present, can be separated in two types respective to their origin.

1. Tangential distortion, prominent in both the Blue and the OH* imagery is caused by the refraction of light through the quartz glass window. A schematic illustration of the effect is shown in figure 10.

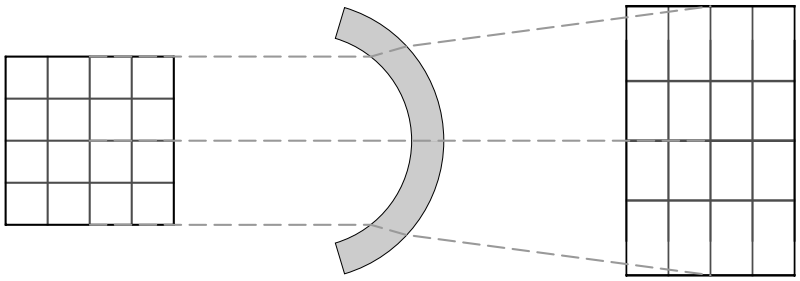

Figure 10.: Tangential glass window distortion

2. Radial distortion, caused by the image intensifier mounted in between the camera lens and the OH* high-speed camera, is present in the OH* imagery. A schematic illustration of the radial pincushion distortion is shown in figure 11.

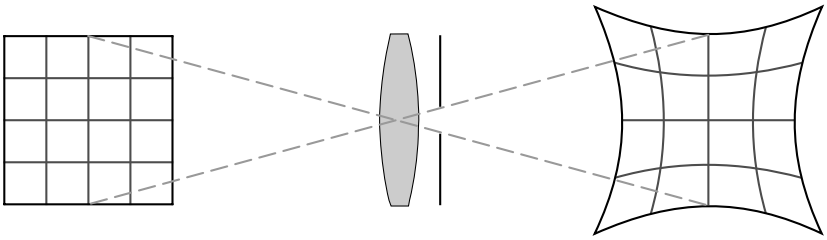

Figure 11.: Pincushion radial distortion

In a first preprocessing step, the OH* imagery is corrected for the radial distortion using the 'Division Model', described by FITZGIBBON [26] to match the Blue imagery.
A sample frame, displayed in false colours, with and without radial distortion correction can be found in figures 12a and 12b respectively.

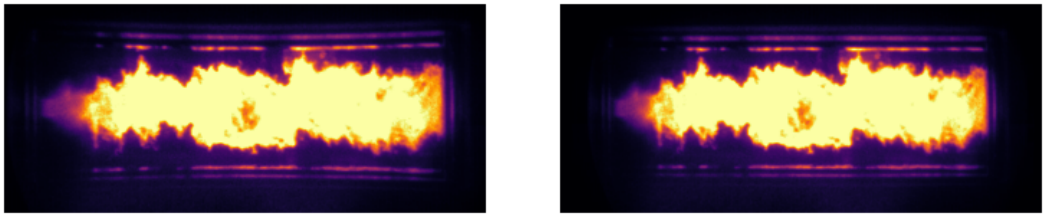

(a) Unprocessed distorted frame

(b) Radial distortion corrected frame

Figure 12.: Correction of radial distortion

Tangential distortion was measured to have parabolic characteristics and is therefore corrected with a parabolic distortion correction. A sample frame, cropped to the window dimensions, can be found in Figure 13, with Figure 13a showing the cropped distorted and Figure 13b the final result.

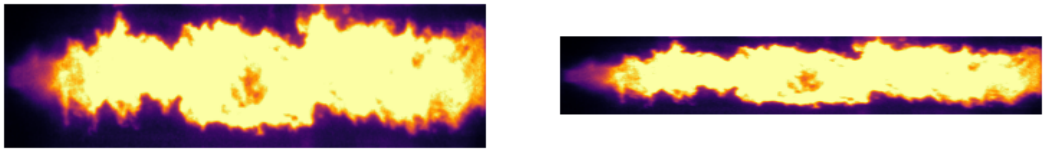

(a) Cropped frame

(b) Tangential distortion corrected frame

Figure 13.: Correction of tangential distortion

4.2. Static Evaluation

To study the flame topology in a static manner, time averaged images were calculated over periods of 0.25 s. Example time averaged images are shown in Figure 14.

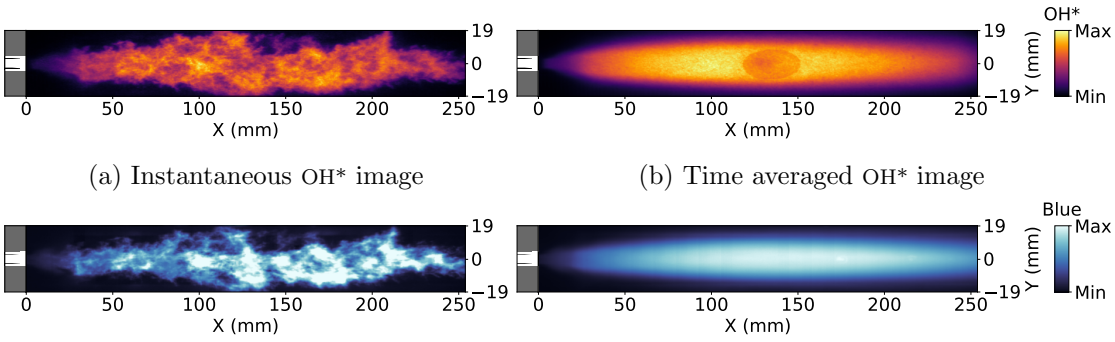

(a) Instantaneous OH* image

(b) Time averaged OH* image

(c) Instantaneous Blue image

(d) Time averaged Blue image

Figure 14.: Time averaged images

Consequently, two different approaches were taken to analyse the mean frames:

1. A flame detection algorithm was implemented to binarise the images and study the flame shape.

2. Intensity profiles were evaluated to study the extent of the flame.

As pointed out in Section 2.3, Fiala et al. found that the flame structure of OH* and Blue imagery is quite similar [14]. Nevertheless, it turned out that for both approaches one type of recording was better suited in each case.

The OH* imagery is characterised by concise contours, compared to the Blue imagery in which the contours appear rather blurry. This makes the OH* imagery better suited for a flame detection algorithm. Furthermore, reflections from the window are present in the Blue imagery rendering it almost useless for automatised flame detection.

However, at certain operating conditions the flame extends beyond the window dimensions and flame detection is therefore not suited for analysis of the flame length and width. To compare these trades, intensity profiles of the Blue imagery were calculated. Blue imagery was selected because, as Fiala et al. pointed out, Blue radiation suffers

from less self-absorption than OH* [14]. The self-absorption falsifies the structure as only the outer flame surface is recorded and therefore makes the intensity profiles less meaningful.

4.2.1. Flame Detection - Opening Characteristics

To study the flame opening behaviour, a flame detection algorithm was used on the OH* imagery to extract the shape. In order to retrieve the flame contour, a simple thresholding was performed to binarise the imagery. To improve the detection, the frames were further processed, by equalising the histogram and artificially increasing the sharpness before thresholding. Additionally, the brightness was increased with a gradient from left to right, to compensate for the low intensity near the injection plane. An example of the flame detection can be found in figure 15.

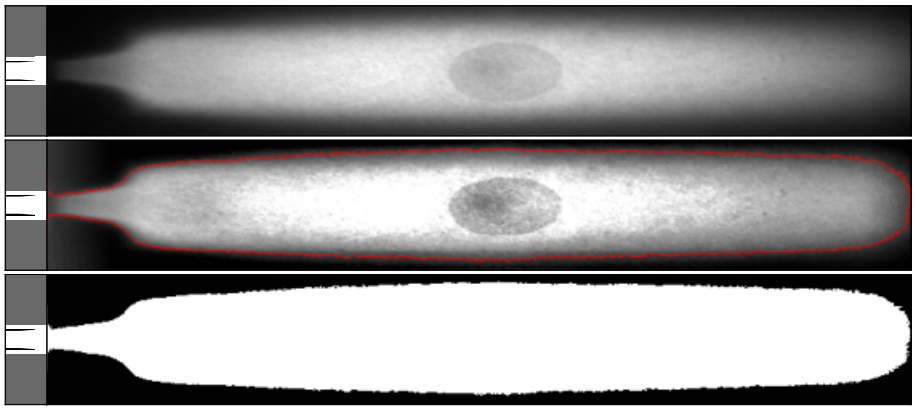

Figure 15.: Flame detection showcase of OH* imagery: Preprocessed frame (top), further-processed frame with the threshold indicated in red (middle) and binarised result (bottom).

Two angles were defined to characterise the opening behaviour. Therefore, a linear fit using least mean squares was used to model the flame contour between 2%-7% of the window length. The angle between the upper and lower fitted contour line has been defined as the *spread angle* (α) in the following. The same was done for the area between 8.5%-11% and defined as *bloom angle* (β). An illustration visualising the two angles in a binarised image is depicted in Figure 16.

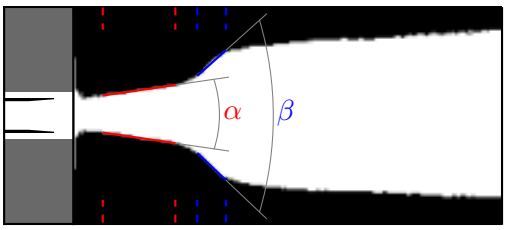

Figure 16.: Visualisation of spread and bloom angle

4.2.2. Axial Intensity Profiles - Length

Axial intensity profiles were calculated for the Blue imagery, to compare the flame length. In order to make imagery comparable, the intensity profiles were normalised by the maximum intensity of each frame. Two different regions of interest (ROI) were investigated: The whole window height, denoted as *Whole window* and 45%-55% of the window height, denoted as *Centerline*. A sample frame with the ROI indicated and the corresponding intensity profiles can be found in Figure 17. In the *Whole window* profile the flame width is also taken into account. This can be seen at the distinct edge in the intensity profile at around 30 mm, where the flame opens up.

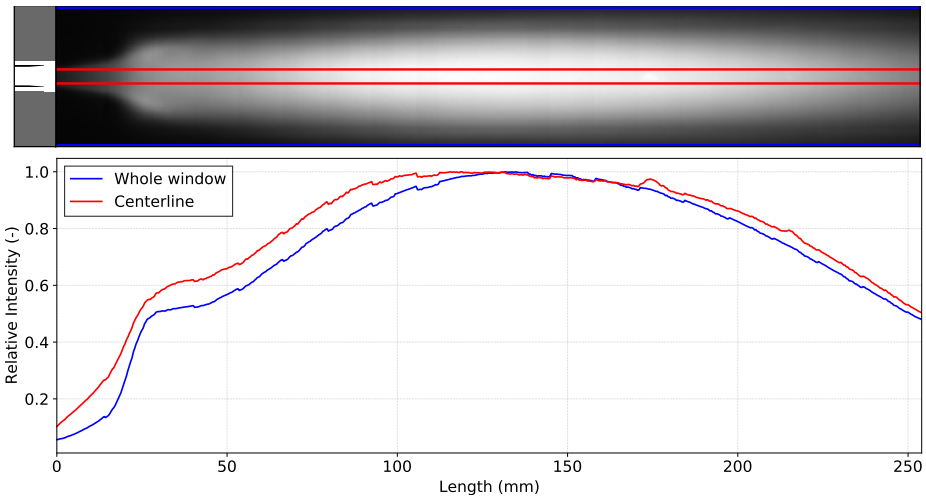

Figure 17.: Axial intensity profiles of Blue imagery

Therefore, the *Centerline* region of interest is used for length comparison, to not take the width into account. A similar study conducted by Suslov et al. used a threshold

of 50% maximum intensity as definition of the flame length [18]. However, as mentioned above, at certain operating conditions the flame extends way beyond the window length and 50% of maximum intensity is not reached. Hence the length was defined by 80% of maximum intensity for this study.

4.2.3. Radial Intensity Profiles - Width

Similar to the axial intensity profiles, radial intensity profiles were calculated for different ROI to investigate the radial extent of the flame. The width has been defined as 50% of the maximum intensity present in each ROI. A sample frame showing five regions of interest and the corresponding radial intensity profiles is depicted in Figure 18.

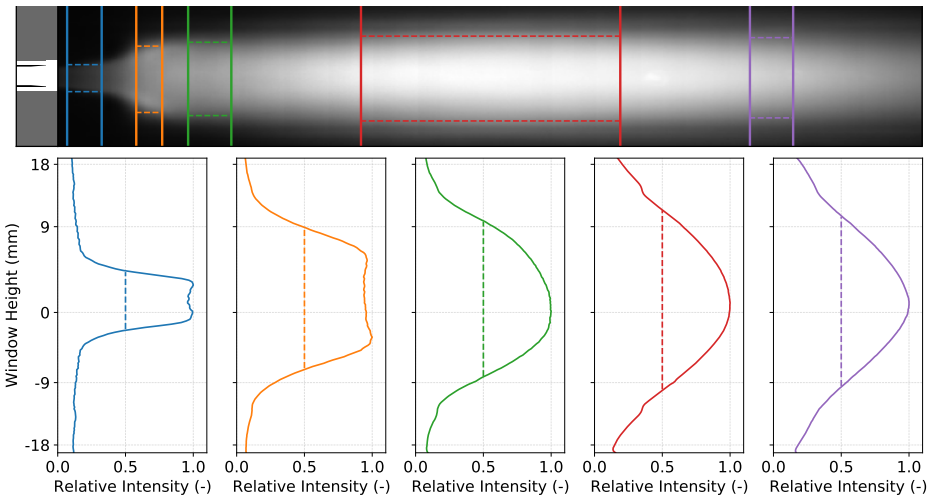

Figure 18.: Radial intensity profiles of Blue imagery

4.3. Dynamic Evaluation

The main focus of the second part of the analysis is to investigate the flame dynamics at certain frequencies. As the particular combustion chamber BKN has not been part of any previous study, the origin of the appearing oscillations and their corresponding frequencies needs to be identified. The flame response is then analysed in a second step.

4.3.1. Dynamic Mode Decomposition

To investigate the flame response to pressure oscillations at certain frequencies, DMD was applied to the optical data. The DMD is a dimensionality reduction method, whose advantage is to be selective in frequency. The method was introduced by Schmid [27] and has been used in various previous investigations of dynamic flame behaviour [16, 25, 28, 17].

The multi-variable DMD method uses the same DMD method as described by SCHMID [27], but it integrates different diagnostics and measurements to create the DMD data matrix. Thereby, the method allows to decompose different types of measurements simultaneously. A single spatial snapshot of the DMD data matrix is created from the simultaneously recorded imagery and pressure data.

The optical data from one snapshot in time is arranged in one column and the dynamic pressure data is appended to the data matrix as additional spatial points for each temporal snapshot. The calculated DMD modes serve as a common basis for all variables used in the DMD calculation. Once the DMD is computed, the points in the DMD modes corresponding to each variable can be separated and reordered to match the original input data. BEINKE et al. previously used the multi-variable DMD approach to analyze combustion instability data [16]. In the thesis at hand, the multi-variable DMD was applied to process simultaneously recorded dynamic pressure sensor data with the OH* and Blue optical data samples from BKN. A schematic illustration of the mulit-variable DMD can be found in Figure 19.

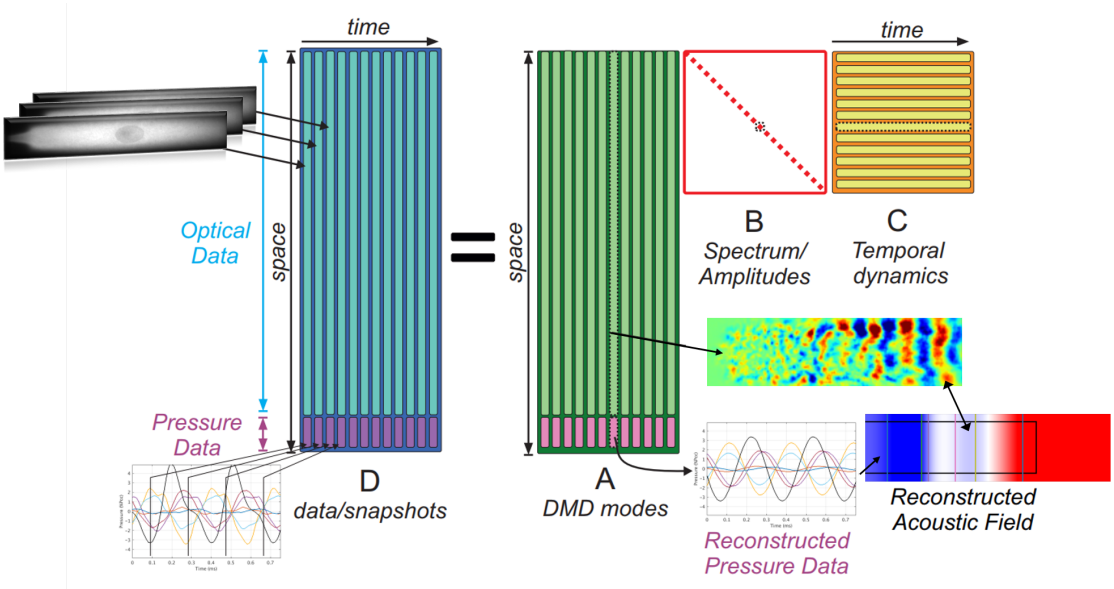

Figure 19.: Application of multi-variable DMD method to BKN experimental data (based on [16])

4.3.2. Pressure Field Reconstruction

The pressure field was reconstructed from the dynamic pressure sensors, spread along the chamber axis, by applying a spline interpolation. For this closed-closed boundary conditions were implemented on the injection plane and nozzle.

5. Results and Discussion

The results obtained in the investigation are presented in this chapter.

5.1. Anomalies

A number of anomalies appeared in the measurement data. The two particularly influencing this investigation shall be addressed in this section.

OH* Intensifier Artefact

The most obvious anomaly is present in the OH* imagery as a a circular area with reduced intensity. It is especially prominent in time averaged images and can be seen, for example in Figure 15. It was caused by a defect in the OH* intensifier. The artefact is not known to have any influence on the results of the study at hand, apart from catching the eye.

Overexposed Imagery for 07run3

In the first test both types of radiation imagery were overexposed, resulting in a clipping of high intensities. An example can be seen in Figure 13 where the central area of the flame has a constant intensity. The clipping caused the radial intensity profiles to take a significantly different shape, compromising the comparability to a certain extent.

5.2. Flame Topology

The unique window size allows for extensive analysis of the flame topology. The corresponding findings are detailed in this subsection.

5.2.1. OH* vs. Blue Radiation

In the first part of the topology evaluation the OH* and Blue imagery are compared. Split frames showing OH* radiation at the top and Blue radiation at the bottom for LP 4 are depicted in Figure 20. Similar comparison frames for the all LPs can be found in Appendix A.2. The general flame shape appears to be very similar for both types of radiation throughout all load points, for instantaneous as well as time averaged imagery. This coincides with the observations made by Fiala et al., expounded in Section 2.3.

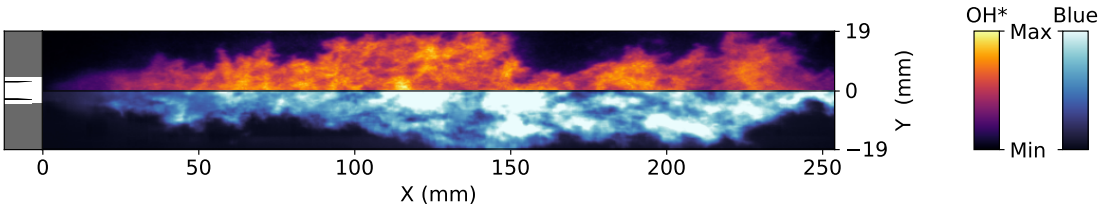

(a) Instantaneous OH* and Blue image

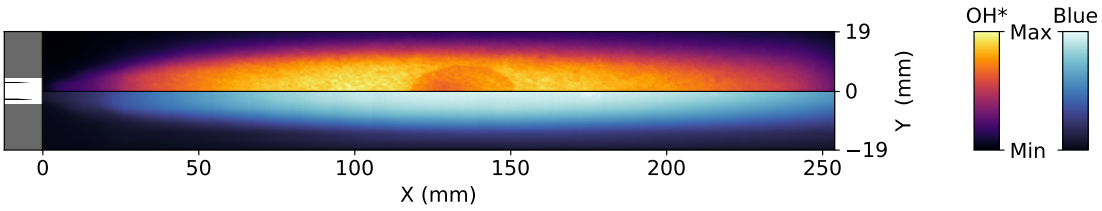

(b) Time averaged OH* and Blue image

Figure 20.: Comparison of OH* and Blue imagery at LP 4

In contrast to the flame shape, the flame structure varies significantly between the two types of radiation in the instantaneous imagery. Areas of maximum intensity appear in different regions of the flame. This can most likely be traced back to the stronger self absorption of the OH* radiation.

5.2.2. Reproducibility

The flame shape was analysed with a flame detection algorithm applied to the OH* imagery, as described in 4. As detailed in 3.1.3, the LPs 2 and 4 were realised in test run 07run3 as well as 07run5. Comparisons of the flame shapes at the same LPs in different test runs are depicted in Figure 21.

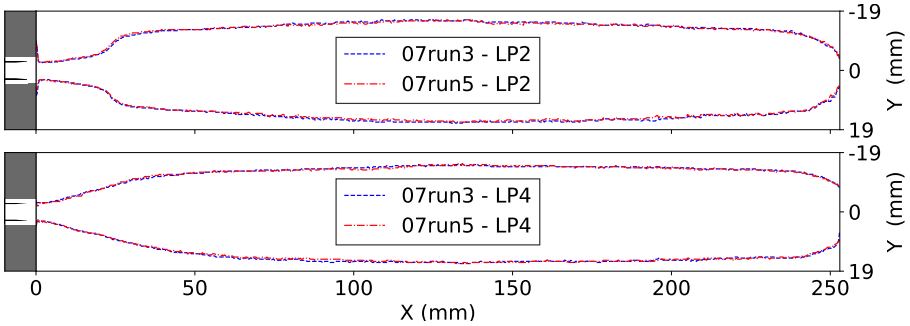

Figure 21.: Flame shape comparison

Independent of varying camera settings, the detected flame shapes are nearly identical for similar injection and operating conditions, indicating a great reproducibility. Therefore, the data allows for the evaluation of the flame shape across different test runs.

5.2.3. Opening Characteristics

To study the opening behaviour of the flame, the shape was analysed in the first 75 mm of the window length. The outer shape of the flame in bespoken area is referred to as *opening profile* in the following. A comparison of the opening profiles for LP 1 and LP 4 as well as LP 2 and LP 3 can be found in Figure 22a and Figure 22b, respectively. In direct comparison it can be observed that at higher J-numbers in Figure 22a the flame rapidly occupies a large volume, indicating that the LOX jet breakup and mixing is faster compared to lower J-numbers in Figure 22b. This can be traced back to the shear forces between the LOX core and co-flowing H_2 increasing with rising J. Given the relatively stable propellant temperatures and combustion chamber pressures throughout all four supercritical load points, the momentum flux ratio is merely dependent on the VR. Therefore it can be observed, that the flame departs earlier from the core region if the relative velocity of hydrogen to oxygen is increased. Additionally, the widening

of the flame appears rather sudden at lower J-numbers, which is prominent in the high blooming angle of the opening profiles in 22b. The same behaviour can be observed in between the LPs lying close together, even though less significant.

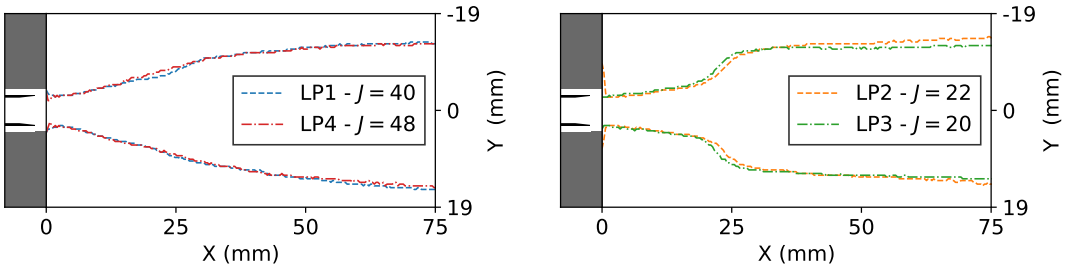

(a) Opening profiles at LP 1 and LP 4

(b) Opening profiles at LP 2 and LP 3

Figure 22.: Opening profiles at supercritical LPs

Figure 23 shows the opening profiles at LP 3 and LP 4 compared to the subcritical LP 5. At LP 5 the momentum flux ratio exceeds the values of the supercritical LPs by far. This results in even higher shear forces and an even earlier LOX core disintegration, visible in the bulge present at around 10 mm to 25 mm. The flame seems to contract again after the bulge and only completely expend further downstream strongly asymmetrically. This might be due to the different atomisation process in the subcritical regime. However, the extremely high momentum flux ratio might also play a significant role. As high pressure H_2/O_2 combustion with J-numbers in similar magnitudes has not been studied before, results from other studies for a comparison are lacking.

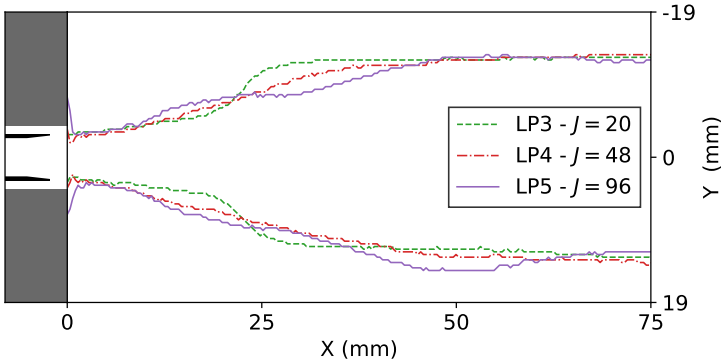

Figure 23.: Opening profiles at LP 3, LP 4 and LP 5

To investigate the opening behaviour in a quantitative manner, spread and bloom angles were calculated as elaborated in 4.2. The spread angle is presumably dependent on the length of the flame following the LOX core and the bloom angle could be defined by the expansion of the flame due to LOX core disintegration. The corresponding angles are plotted in Figure 24 over the momentum flux ratio for all load points. Additionally, data from test run 07run3 recorded in between the LPs is shown in grey.

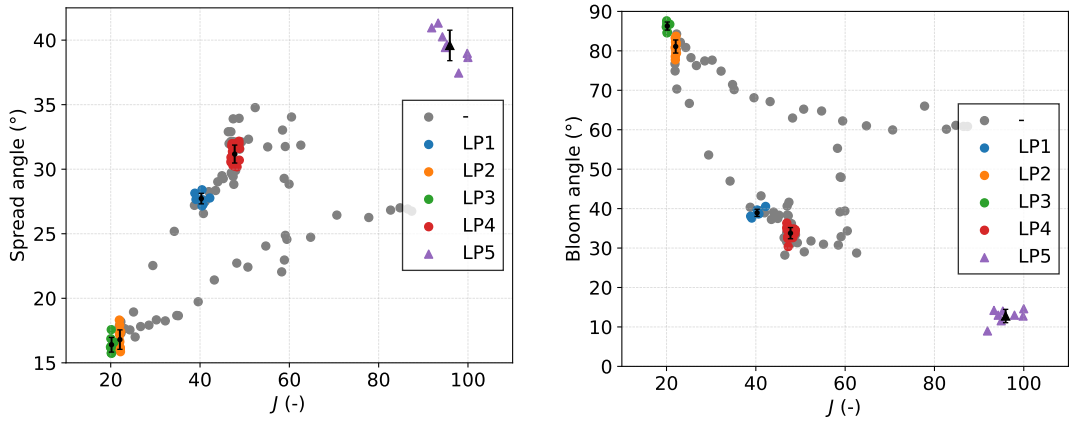

(a) Spread angle vs. J

(b) Bloom angle vs. J

Figure 24.: Opening angles vs. momentum flux ratio

In between the supercritical load points with relatively constant pressure, the spread angle increases almost linear with the momentum flux ratio. The spread angle also seems to decrease with falling pressure. This can be seen in the lower almost linearly line of grey data points, which ran through the same ROF as the upper curve but with constantly decreasing pressure, before the flame quenched. Another observation can be made in the almost straight vertical line of data points around $J = 58$, where the combustion was ramped up at a nearly constant momentum flux ratio. The spread angle was found to increase with rising total momentum flux and chamber pressure.

The bloom angle behaves opposite to the spread angle, although in a rather logarithmic than linear manner. Both angles are identical at LP 4 implying an almost perfectly linear flame opening.

In summary, it was found that the spread angle increases and the bloom angle decreases with rising J. However the influence of chamber pressure and total momentum flux needs to be investigated in future experiments to concretise the respective effects. The same holds true for the subcritical load point as it seems to fit the proposed correlation, but more data points would be needed to affirm.

5.2.4. Flame Length

The flame length has been defined in 4.2.2 as 80 % of the maximum intensity in the centre area. The identified flame lengths are plotted against the corresponding momentum flux ratios in Figure 25. As detailed in 3.1.3, the ROF was changed between the supercritical load points by varying the H_2 mass flow, while the O_2 mass flow was kept nearly constant. Here, the length first sees a significant drop with a small increase in the J-number from LP 3 to LP 2. This seems to be in compliance with the findings of SUSLOV et al. [18]. Even though SUSLOV et al. investigated the LOX core length, it is strongly linked to the overall flame length. However the flame length increases again with rising momentum flux ratio beyond $J = 22$. This contradicts the findings made by SUSLOV et al., but is most likely due to the momentum flux ratios investigated here being magnitudes higher than in bespoken study. Additionally, the LOX core length is not necessarily similar to the actual flame length, also complicating the comparison.

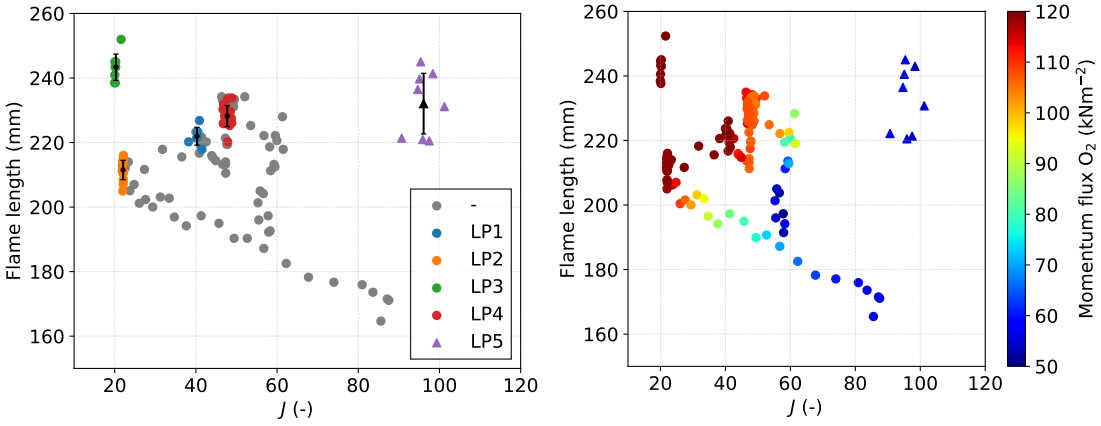

(a) Flame length vs. J

(b) Flame length vs. J vs. O_2 momentum flux

Figure 25.: Flame length at 80% intensity vs. momentum flux ratio

Besides the load points where the oxygen mass flow stayed constant, $\dot{m}_{O_2}$ was varied on ramp up and ramp down. The results show, that the flame length is significantly influenced by the absolute momentum flux of the LOX core, which seems intuitive as with a higher momentum the flame should extend further. This is clearly visible in Figure 25b where the flame length is additionally overlayed with the corresponding O_2 momentum flux. During the ramp up, J has been kept almost constant at around $J = 58$ and the flame length increased with rising LOX core momentum. The same can be observed on the ramp down, where similar J-numbers were run through as in the supercritical load points discussed above. The flame length however, keeps decreasing while J increases.

Another interesting finding is the dip of the flame length between LP 1 and LP 4. The window cooling mass flow was ramped up between the two steady points resulting in a quite significant decrease in flame length. Due to the sharp drop between LP 3 and LP 2 where the window cooling mass flow and lox momentum are almost constant, it is assumed that the J number has a more significant impact on flame length at smaller J-numbers. Because data from comparable window lengths and J-numbers are non existent the investigation at hand lacks comparison. At first glance no clear dependency can be derived from the measured results. Therefore, more investigations need to be conducted to identify the interaction of J, lox core momentum and window cooling for sub and supercritical conditions at similar momentum flux ratios.

5.2.5. Flame Width

To study the radial extension of the flame, it's width was determined as 50% of the maximum intensity as described in 4.2.3. The width of a central region of interest from 35% to 85% of the window length is plotted against the momentum flux ratio in Figure 26. The width initially increases with rising J from LP 3 to LP 2, but above $J = 22$ the central flame width seems to collapse almost linearly with further increase of the momentum flux ratio. Lower ROF and thus higher J-numbers lead to the ROF_{bulk} in the combustion chamber being lower and therefore leaves more unburnt hydrogen in the combustion chamber which constricts the flame. It should be noted however, that there is a significant divergence of calculated flame width at identical load points between the test runs. This is due to the overexposure of the imagery from test run 07run3 detailed in 5.1, which seems to have a significant impact on intensity profiles in the given ROI.

Therefore, the width is difficult to compare between the different test runs in an absolute

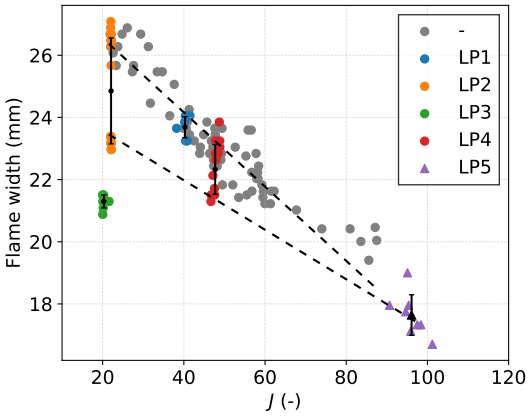

Figure 26.: Flame width vs. momentum flux ratio

manner. Nevertheless, the grey data points all originate from the same test run and the linear behaviour seems to be consistent even in the other test runs where no clipping appeared, as indicated with the dotted lines. However, as mentioned above, LP 3 falls through the cracks. The correlation seems to reverse at lower J-numbers. The rise from LP 3 to LP 2 is quite significant indicating a higher influence of J-number on the flame width at lower momentum flux ratios. The findings should be treated with caution as the radial extension would notably change in a multi-injector combustor.

5.3. Acoustic Characteristics

The identification of the excited acoustic modes present in the dynamic pressure data is crucial for this study and is attempted in the following. As the imagery was recorded with 20,000 fps, the dynamic analysis of the investigation at hand covers only the spectrum below the NYQUIST frequency of 10 kHz to prevent aliasing.

Combustion Chamber Modes

The analytic Equation 10 for linear acoustic eigenmodes in a cylindrical volume is used to estimate the frequencies f of different combustion chamber modes [4]:

$$f_{m,n,q} = \frac{c(\eta_{c*})}{2}\sqrt{\left(\frac{\alpha_{mn}}{R}\right)^2 + \left(\frac{q}{L}\right)^2} \tag{10}$$

Here, the variable $c(\eta_{c*})$ is the equilibrium speed of sound in the combustion chamber, calculated with NASA CEA [29] with dependence on the combustion efficiency η_{c*}. R denotes the radius of the chamber and L the length from injector plane to throat. The variables m,n and q indicate the order for the radial, tangential and longitudinal modes respectively. α_{mn} is the mth root of the radial derivation of the nth order Bessel function of first kind divided by π. A visualisation of the first order modes in a cylindrical volume can be found in Figure 27.

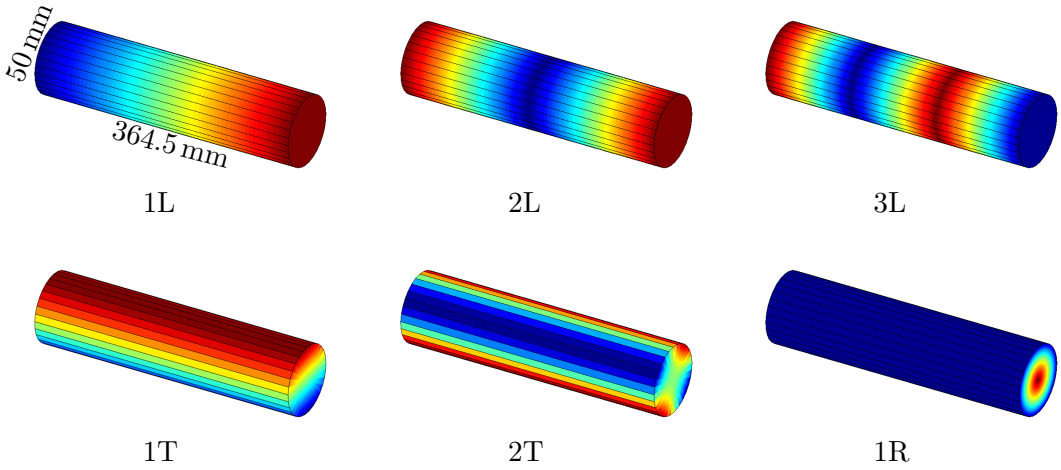

Figure 27.: Pressure distributions for the resonance modes of a simple cylindrical volume

Equation 10 was used to calculate the first order chamber modes. This was done to get an estimate of which modes could appear below 10 kHz. The calculation neglects the flow in the chamber, assumes a homogeneous sound velocity field and implies a perfect sound-hard boundary condition at faceplate and nozzle throat. Despite these simplifications, the calculation allows for an estimate of the chamber modes. Assuming a typical H_2/O_2 combustion efficiency of $\eta_{c*} = 0.95$ [5] and using conditions present at LP 4 during test run 07run5 Equation 10 results in the frequencies listed in Table 4. Therefore, it This narrows the appearance of chamber modes below 10 kHz to the first longitudinal and it's primary three overtones.

Table 4.: Theoretical mode frequencies for basic BKN chamber dimensions

Mode Name	Label	Frequency (Hz)
First Longitudinal	1L	2366
First Tangential	1T	20,219
First Combined	1L1T	20,765
First Radial	1R	42,094

LOX Post Resonance Modes

Previous investigations found, that besides the chamber eigenmodes, the longitudinal modes of the lox post are commonly present in the combustion chamber as well [8, 17]. The LOX-post resonance frequencies can be calculated using the formula for an open-open tube, with an injector length correction of $\Delta L = 0.8d$. The correction was introduced by DRANOVSKY et al. [12] and can be found in Equation 11.

$$f_{nLOX} = \frac{n \cdot c_{LOX}}{2(L + \Delta L)} \tag{11}$$

With the conditions present at LP 4, similar to the calculations above and a sound speed of oxygen c_{LOX} calculated with COOLPROP [30], the equation yields a result of $f_{1LOX} = 2839\,\text{Hz}$.

Acoustic Mode Identification

In Figure 28 power spectral density (PSD) plots of dynamic pressure sensor data in the combustion chamber, oxygen and hydrogen injection manifolds are presented. The PSDs

were calculated using a 50% overlap and Hamming window with a 10 Hz resolution, over a period of one second during LP 4 conditions in test run 07run5. The frequencies, analytically calculated above are also indicated in Figure 28.

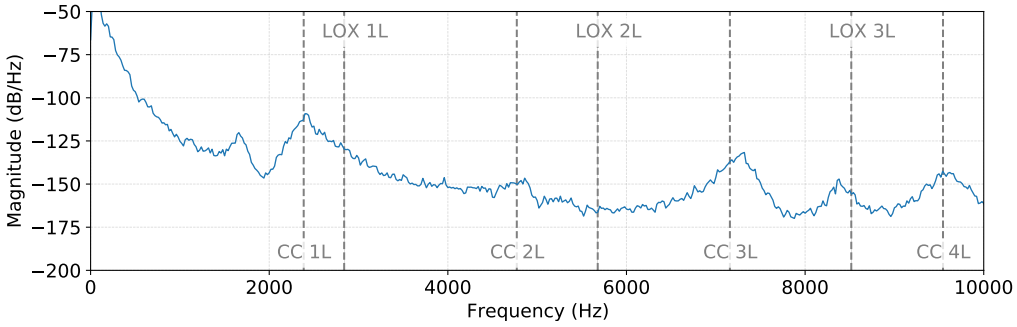

(a) PSD of PCCdyn2 (in combustion chamber)

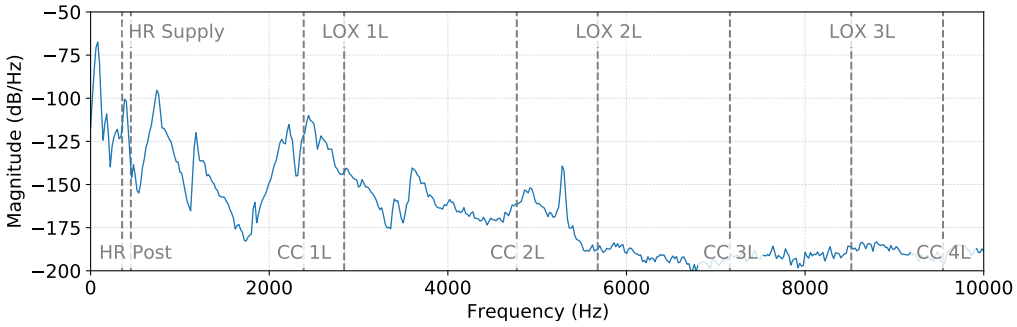

(b) PSD of PIOdyn2 (in O_2 injection manifold)

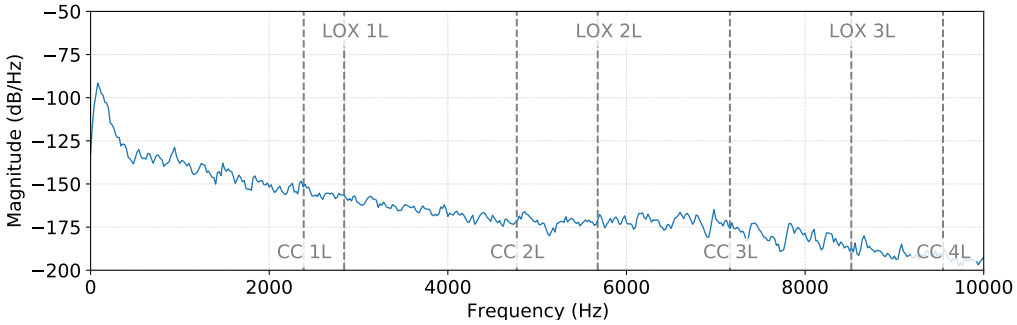

(c) PSD of PIFdyn1 (in H_2 injection manifold)

Figure 28.: PSD Plots of multiple dynamic pressure sensor and analytically calculated frequencies

In Figure 28a four peaks match the first longitudinal of the chamber and its overtones.

Therefore, it is assumed that these peaks originate from the chamber eigenmode. Another peak matches the third LOX-post frequency. The LOX-post eigenmode could be the origin of the peak in the dynamic pressure data. However the first and second LOX-post modes do not show any excitation. Another peak at around 1600 Hz has been identified as a sensor artefact and is consequently not addressed in the following.

The identification of the peaks in the LOX-dome, on the other hand, is more difficult. Peaks near the analytically calculated 1L and 2L of the combustion chamber are present. However they need to be further investigated to confirm their origin. The first three prominent peaks might be caused, by the LOX-dome acting as a HELMHOLTZ resonator. HELMHOLTZ resonators are acoustic cavities connected with a small passage. The resonance frequency of a given resonator can be calculated with Equation 12 [31].

$$f_{HR} = \frac{c_{LOX}}{2\pi}\sqrt{\frac{A}{V(L+\Delta L)}} \tag{12}$$

With V denoting the volume of the resonator and A the area of the passage. The equation yields a frequency of 345 Hz for the post acting as the passage and frequency of 452 Hz for the supply line acting as the passage. The frequencies are also indicated in 28b. Bespoken frequencies and their overtones seem to fit the first three peaks in the PSD of the LOX-dome. Nevertheless, the hypothesis needs to be investigated further in future studies.

No prominent peaks are present in the hydrogen dome PSD, shown in 28c. Hence, it can be assumed that oscillations from the combustion chamber do not propagate upstream the fuel injector.

5.4. Dynamics

High-speed imagery and dynamic pressure data have been used to investigate the dynamic behaviour of the flame. The two test runs in which imagery has been obtained at a sufficiently high frame rates to investigate the dynamics, are shown in Figure 29. The test runs are described with spectrograms (top) of the unsteady pressure signal (middle), along with the test sequence (bottom).

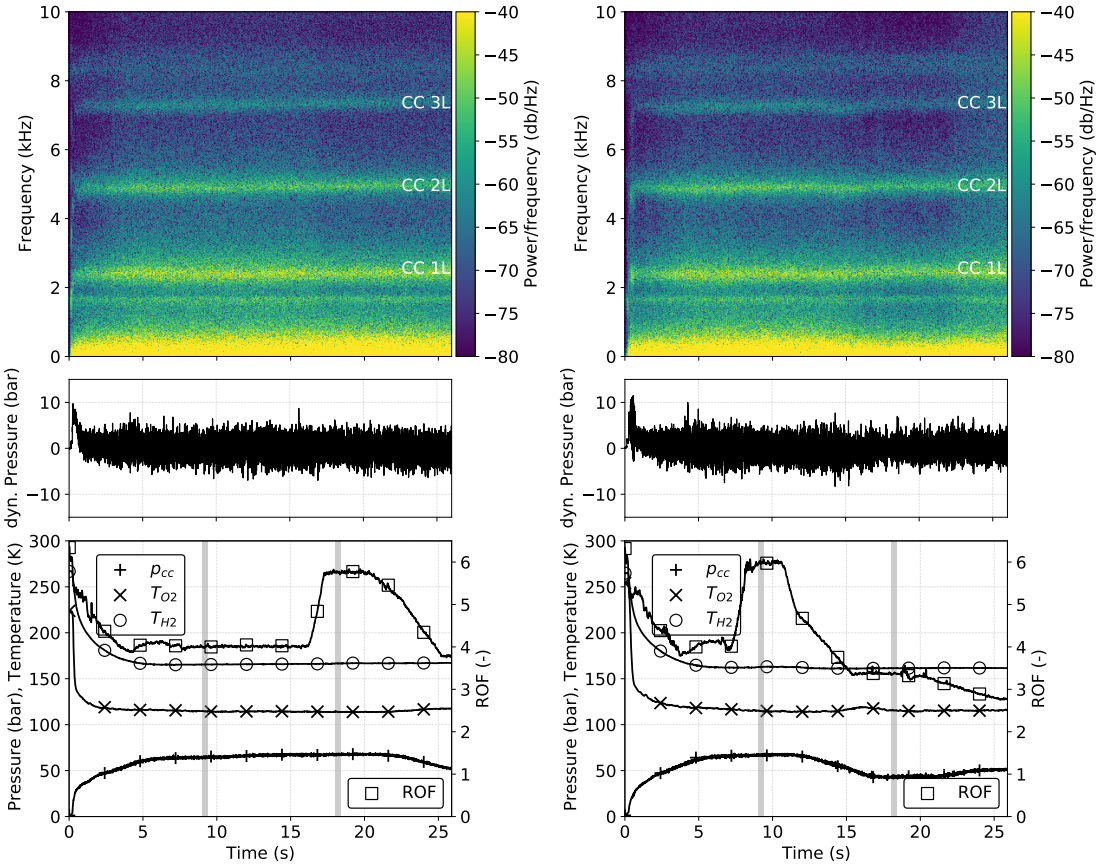

(a) 07run5 (b) 07run7

Figure 29.: Test sequence with operating conditions (bottom), unsteady pressure trace of PCCdyn2 (middle), and spectrogram from unsteady pressure (top)

The identified chamber modes are also labelled in the spectrograms. The raw pressure signal (middle) and the spectrogram (top) describe the stability character of the combus-

tion process. The DMD was performed on the intervals, which are highlighted in grey in the test sequences (bottom). No prominent instabilities appeared neither of the test runs, as the pressure data in Figure 29 shows. The combustion appears to be relatively stable throughout all employed operating conditions. Furthermore, the frequencies of the oscillations at the longitudinal chamber modes seem to be almost independent of the operating conditions, matching observations made in other combustors [8, 32]. This might be due to a damping effect of the window cooling mass flow, as the combustion chamber frequencies are mainly dependent on the ROF and the ROF_{bulk} in BKN varies only slightly due to the massive cooling film. Nevertheless, the dynamic behaviour of test run 07run5 and the corresponding load points 2 and 4 are further examined in this investigation.

5.4.1. Dynamic Mode Decomposition

For the multi-variable DMD 2000 images comprising a 0.1 s interval were processed for each load point yielding a resolution of 10 Hz. Before each interval the operating conditions were already kept constant for 2 s to ensure no transient effects are present. Figure 30 shows the calculated DMD mode magnitudes for the OH* and Blue imagery.

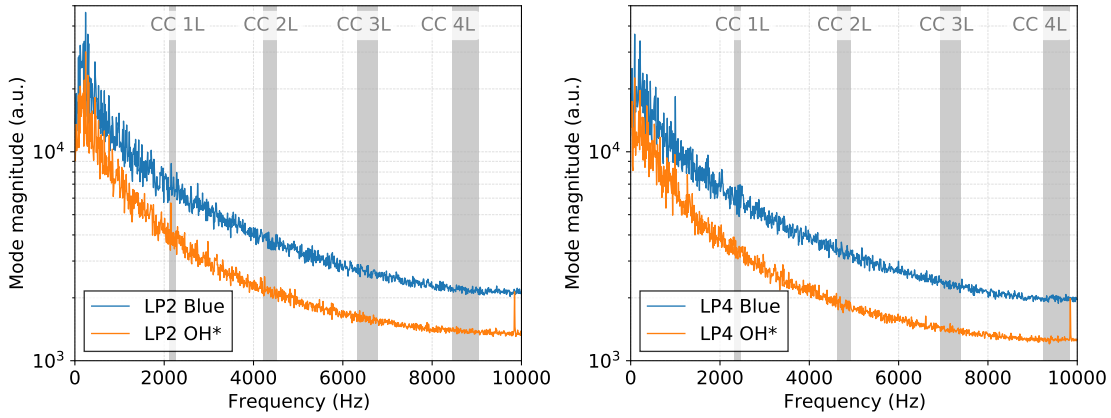

(a) Load point 2

(b) Load point 4

Figure 30.: DMD mode magnitude over frequency

As expected the output of the DMD shows no significant peaks indicating a notable unstable behaviour. However a number of interesting modes are still present in the

data. In Figure 30a showing the results for LP 2, a sharp, even though not particularly high peak is present at 2160 Hz in the area where the first longitudinal eigenmode of the combustion chamber is predicted. The 1L chamber mode being more prominent in LP2 is in compliance with previous studies, which found, that the excitation of the chamber modes is more likely at high ROF [32]. The results of the DMD for this frequency are further expounded in 5.4.2. The DMD mode magnitudes for LP 4 on the other hand show no response at the chamber eigenmodes. However prominent peaks are present at 500 Hz and 1000 Hz. Their origin and the corresponding effects are investigated in 5.4.3. Furthermore, the OH* data of the DMD modes show a sharp peak close to 10000 Hz which is suspected to be an artefact of the optical setup.

5.4.2. 1L Combustion Chamber Mode

The reconstructed spatial distribution of the DMD mode at 2510 Hz for LP 2 is depicted in Figure 31. The reconstructed flame shows a similar behaviour in the OH* and Blue imagery. Fluctuations of the flame intensity in the rear part of the flame are most likely caused by oscillations in the injection mass flow.

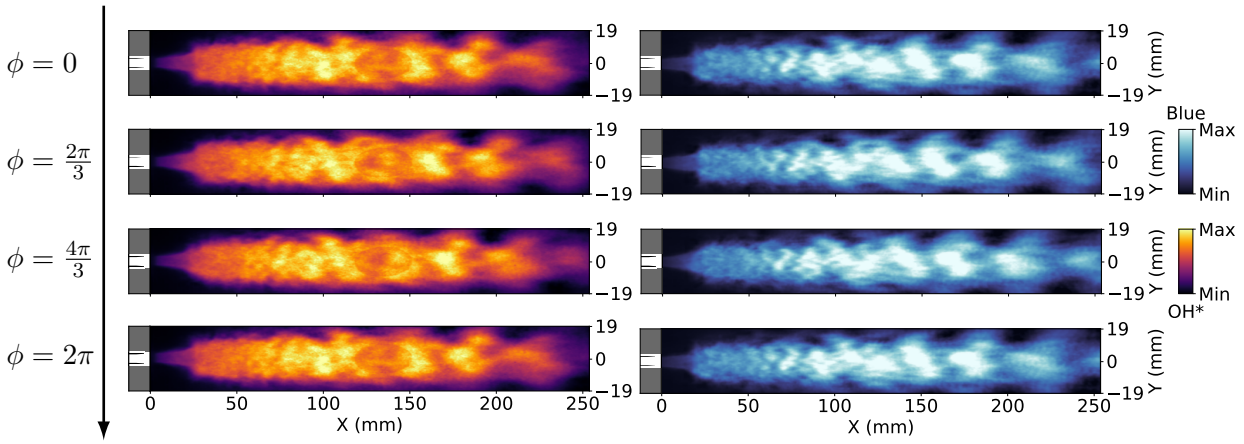

(a) OH* (b) Blue

Figure 31.: Reconstruction of spatial distribution of the DMD mode at 2150 Hz

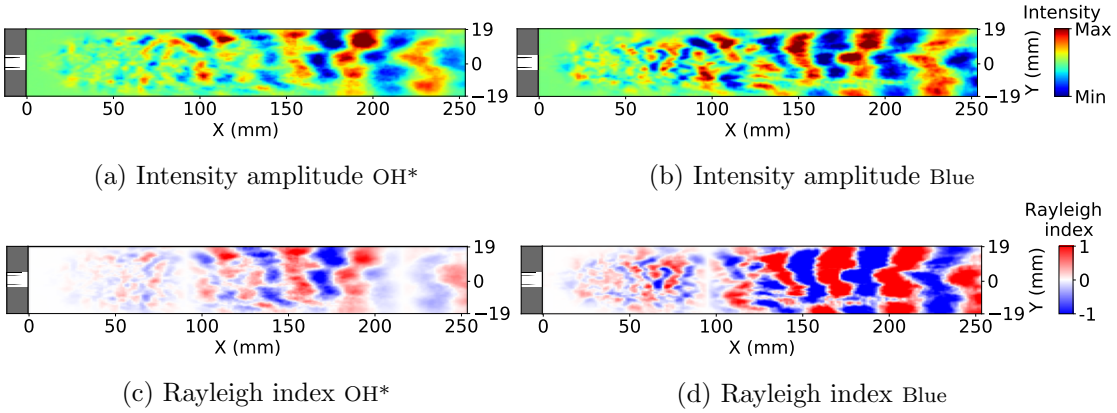

(a) Intensity amplitude OH*

(b) Intensity amplitude Blue

(c) Rayleigh index OH*

(d) Rayleigh index Blue

Figure 32.: Flame response distribution computed for the DMD mode at 2150 Hz

Oscillations of the injection mass flow might result from the pressure oscillation near the injector plane, which reach up to 1.5% of the mean chamber pressure. The calculated results from the multi-variable DMD analysis during 1L mode excitation are shown in Figure 32. The intensity amplitudes plotted for OH* and Blue radiation are shown in Figure 32a and 32b, respectively show a wave-like pattern, corresponding to the predicted oscillations in mass flow. The ridges of the wave-like pattern seem to be in phase with the local acoustic pressure disturbance as they produce positive Rayleigh indices in Figure 32c and Figure 32d. However, boiling cooling water corrupted the measurements of the rear three dynamic pressure sensors to a certain extent. Leaving the Rayleigh indices untrustworthy. This might also explains, why the pressure nodal line does not appear near the centre of the chamber at around 170 mm, where it would be expected for the 1L mode.

5.4.3. Low Frequency Oscillations

The sharp peaks in the DMD mode magnitude PSD, at LP 2 are suspected to be caused by a hydrodynamic effect referred to as natural free jet instability. A non-dimensional relation to analyse vortex shedding frequencies is given by the Strouhal-number (St), defined in Equation 13.

$$St = \frac{f \cdot D_{inj}}{u_{inj}} \tag{13}$$

SCHMID et al. found most interaction of supercritical nitrogen jets occurs at Strouhal-numbers between $0.2-0.4$ [33]. Figure 33 shows simulations of supercritical nitrogen jets, excited at different Strouhal-numbers. Equation 13 yields Strouhal-numbers of 0.21 and 0.42, for the two frequencies prominent in Figure 30b 500 Hz and 1000 Hz, respectively. The reconstructed spatial distribution of the DMD mode at 500 Hz for LP 2 is depicted in Figure 34. Here a movement in the flame similar to the simulated jets in Figure 33 can be observed, contributing to the assumption above.

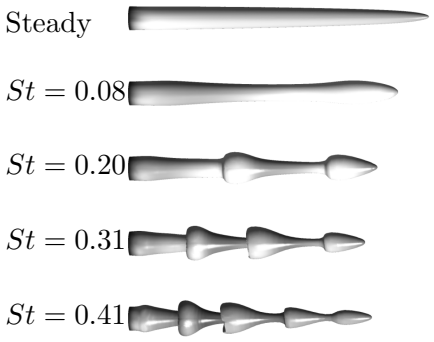

Figure 33.: Simulated supercritical nitrogen jets excited at different Strouhal-numbers [33]

The flame response results from the multi-variable DMD analysis during the 500 Hz mode excitation are depicted in Figure 35. The prospected vortices are clearly visible in the computed intensity distribution plots of the OH* imagery in Figure 35a and the Blue imagery in Figure 35b. They appear as small circular regions of high intensity symmetrically above and below the centre line and travel downstream, where they expand and eventually break apart. Large regions of positive and negative coupling are visible in the Rayleigh index plots for the 500 Hz mode in Figure 35c and Figure 35d. At least visually,

it appears as if the integrated Rayleigh index for OH* at 500 Hz is rather positive. If a combustion chamber mode were in this region, it could possibly be excited.

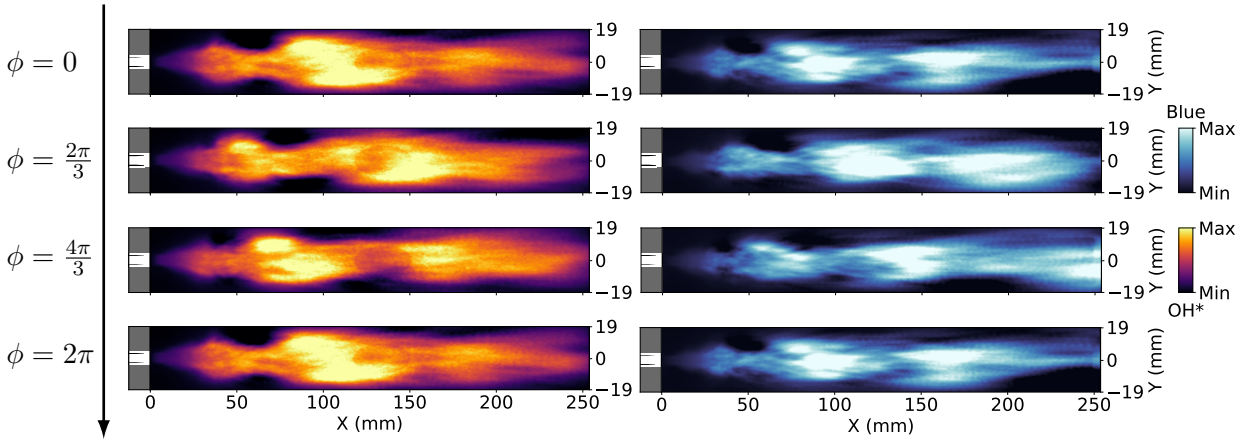

(a) OH* (b) Blue

Figure 34.: Reconstruction of spatial distribution of the DMD mode at 500 Hz

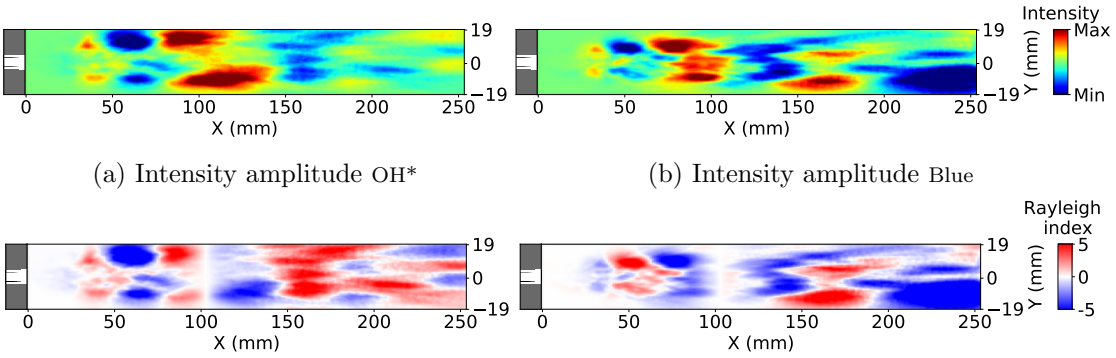

(a) Intensity amplitude OH* (b) Intensity amplitude Blue

(c) Rayleigh index OH* (d) Rayleigh index Blue

Figure 35.: Flame response distribution for the DMD mode at 500 Hz

6. Conclusions and Outlook

High-speed OH* and Blue radiation imagery was used to study the flame phenomenology of a research rocket combustor with a single shear coaxial injector, at injection conditions representative of industrial engines using oxygen–hydrogen propellants. Thereby novel observations were made regarding the flame shape at elevated momentum flux ratios.

Large sets of imagery were time averaged to study the flame topology. The same general flame shape could be observed in both the OH* and Blue imaging. More details in the flame structure could be found in the blue imagery, however the OH* imagery showed more distinct contours. Furthermore, a great reproducability has been achieved across the test runs.

A flame detection algorithm was used to characterise the opening behaviour of the flame. An inverse correlation of the position of flame expansion and the momentum flux ratio was found. This is suspected to be caused by an earlier LOX core break-up due to increased shear forces. Future test campaigns could include shadowgraph imaging to visualise the LOX core and confirm this assumption. The flame length was found to be affected by the momentum flux ratio, LOX jet momentum as well as the window cooling massflow. Due to the limited number of load points, a clear distinction between the influence of each parameter could not be made. The central flame width appeared to collapse above a certain ROF inversely with the momentum flux ratio, most likely due to a constriction by unburned hydrogen. Moreover, the extension of the flame was found to be stronger affected by the momentum flux ratio at higher rates of fuel.

A number of low amplitude oscillations were present in the dynamic data. Through a simple modal analysis, predictions on the driving mechanisms of aforementioned oscillations were made. A multi-variable dynamic mode decomposition was performed on the data to further investigate two of the oscillations. While the first mode was traced back

to be a slight excitation of the first longitudinal eigenmode of the combustion chamber. The source of the second mode is uncertain, although it is suspected to be caused by hydrodynamic effect of the LOX core.

In the course of this thesis, a substantial amount of software was implemented to perform the evaluations presented. This will simplify and accelerate future investigations of test data.

Subsequent test runs could be conducted with additional load points at varying pressures and window cooling massflows, to investigate their individual influence on the flame topology. Additionally, shadowgraph imaging could be used to visualise the oxygen jet and verify the prospected LOX core breakup behaviour. Altering the injector geometry or injection temperatures might provoke instabilities and allow for investigations of the influence of injection parameters on the stability behaviour. The findings highlight the need for further experimental investigations to provide additional information and enhance the current understanding of high pressure combustion.

Bibliography

[1] Turner, M., *Rocket and Spacecraft Propulsion: Principles, Practice and New Developments*, 01 2009.

[2] Sutton, G. and Biblarz, O., *Rocket Propulsion Elements*, A Wiley Interscience publication, Wiley, 2001.

[3] Yang, V., *Liquid Rocket Engine Combustion Instability*, AIAA, Reston, 1995.

[4] Gröning, S., "Untersuchung selbsterregter Verbrennungsinstabilitäten in einer Raketenbrennkammer," Tech. rep., RWTH Aachen, 2017.

[5] Schmidt, G., *Technik der Flüssigkeits-Raketentriebwerke*, DaimlerChrysler Aerospace, 1999.

[6] Messerschmid, E. and Fasoulas, S., *Raumfahrtsysteme, 5., aktualisierte u. erg. Aufl. 2017*, 2017.

[7] Haidn, O., Oschwald, M., Clauss, W., Arnold, R., Sender, J., Preuss, A., Preclik, D., Mäding, C., Görgen, J., and Soller, S., "LOX/Methane Technology Efforts for Future Liquid Rocket Engines," *5th International Spacecraft Propulsion Conference & 2nd International Symposium on Propulsion for Space Transportation*, Mai 2008.

[8] Hardi, J., *Experimental Investigation of High Frequency Combustion Instability in Rocket Engines*, Ph.D. thesis, 01 2012.

[9] Harrje, D., *Liquid Propellant Rocket Combustion Instability*, NASA SP, Scientific and Technical Information Office, National Aeronautics and Space Administration, 1972.

[10] Rayleigh, John S., "The Explanation of Certain Acoustical Phenomena," *Nature*, Vol. 18, No. 455, Jul 1878, pp. 319–321.

[11] Putnam, A. A. and Dennis, W. R., "Organ-pipe oscillations in a flame-filled tube," *Symposium (International) on Combustion*, Vol. 4, No. 1, 1953, pp. 566–575, Fourth Symposium (International) on Combustion.

[12] Dranovsky, M., Yang, V., Culick, F., Talley, D., of Aeronautics, A. I., and Astronautics, *Combustion Instabilities in Liquid Rocket Engines: Testing and Development Practices in Russia*, Progress in Astronautics and A, American Institute of Aeronautics and Astronautics, 2007.

[13] Fiala, T., *Radiation from High Pressure Hydrogen-Oxygen Flames and its Use in Assessing Rocket Combustion Instability*, Ph.D. thesis, 07 2015.

[14] Fiala, T., Sattelmayer, T., Gröning, S., Hardi, J., Stützer, R., Webster, S., and Oschwald, M., "Comparison Between Excited Hydroxyl Radical and Blue Radiation from Hydrogen Rocket Combustion," *Journal of Propulsion and Power*, Vol. 33, No. 2, 2017, pp. 490–500.

[15] Webster, S., Hardi, J., and Oschwald, M., "Comparison of Oxygen-hydrogen Combustion Visualision Techniques under Representative Conditions," *Space Propulsion 2016*, 2016.

[16] Beinke, S. K., Hardi, J., Oschwald, M., Banuti, D. T., Karl, S., and Dally, B. B., *Experimental and numerical study of oxygen-hydrogen rocket flame response to transverse acoustic excitation*.

[17] Armbruster, W., Hardi, J. S., Suslov, D., and Oschwald, M., "Injector-Driven Flame Dynamics in a High-Pressure Multi-Element Oxygen–Hydrogen Rocket Thrust Chamber," *Journal of Propulsion and Power*, Vol. 35, No. 3, 2019, pp. 632–644.

[18] Suslov, D., Hardi, J., and Oschwald, M., "Full-length visualisation of liquid oxygen disintegration in a single injector sub-scale rocket combustor," *Aerospace Science and Technology*, Vol. 86, März 2019, pp. 444–454.

[19] Juniper, M., Tripathi, A., Scouflaire, P., Rolon, J.-C., and Candel, S., "Structure of cryogenic flames at elevated pressures," *Proceedings of the Combustion Institute*, Vol. 28, No. 1, 2000, pp. 1103–1109.

[20] Oschwald, M., Schneider, G., and Clauss, W., "Application of Visualization Techniques and Quantitative Optical Diagnostics for the Investigation of Supercritical Jet Atomization," *8th International Symposium on Fluid Control, Mesurmenet and Visualization*, 2005.

[21] Lux, J. and Haidn, O., "Flame Stabilization in High-Pressure Liquid Oxygen/Methane Rocket Engine Combustion," *Journal of Propulsion and Power*, Vol. 25, No. 1, 2009, pp. 15–23.

[22] Smith, J. J., Schneider, G., Suslov, D., Oschwald, M., and Haidn, O., "Steady-state high pressure LOx/H2 rocket engine combustion," *Aerospace Science and Technology*, Vol. 11, No. 1, 2007, pp. 39–47, Propellant combustion phenomena.

[23] Kendrick, D., Herding, G., Scouflaire, P., Rolon, C., and Candel, S., "Effects of a recess on cryogenic flame stabilization," *Combustion and Flame*, Vol. 118, No. 3, 1999, pp. 327–339.

[24] Portal, D., "DLR – P8 test rig at the DLR Lampoldshausen site," .

[25] Hardi, J. S., Beinke, S. K., Oschwald, M., and Dally, B. B., "Coupling of Cryogenic Oxygen–Hydrogen Flames to Longitudinal and Transverse Acoustic Instabilities," *Journal of Propulsion and Power*, Vol. 30, No. 4, 2014, pp. 991–1004.

[26] Fitzgibbon, A., "Simultaneous linear estimation of multiple view geometry and lens distortion," *Proceedings of the 2001 IEEE Computer Society Conference on Computer Vision and Pattern Recognition. CVPR 2001*, Vol. 1, 2001, pp. I–I.

[27] Schmid, P. and Sesterhenn, J., "Dynamic Mode Decomposition of numerical and experimental data," *Journal of Fluid Mechanics*, Vol. 656, 11 2008.

[28] Ristori, A., Hardi, J., Kawashima, H., and Oschwald, M., *Flame response to high-frequency oscillations in a cryogenic oxygen/hydrogen rocket combustor*, 02 2019.

[29] Gordon, S., *Computer Program for Calculation of Complex Chemical Equilibrium Compositions and Applications. Part 1: Analysis*, 1994.

[30] Bell, I. H., Wronski, J., Quoilin, S., and Lemort, V., "Pure and Pseudo-pure Fluid Thermophysical Property Evaluation and the Open-Source Thermophysical Property Library CoolProp," *Industrial & Engineering Chemistry Research*, Vol. 53, No. 6, 2014, pp. 2498–2508.

[31] Jr, A., Silva, M., Lacava, P., and Goes, L., "Acoustic Cavities Design Procedures," *Revista de Engenharia Térmica*, Vol. 6, 09 2018.

[32] Gröning, S., Hardi, J. S., Suslov, D., and Oschwald, M., "Injector-Driven Combustion Instabilities in a Hydrogen/Oxygen Rocket Combustor," *Journal of Propulsion and Power*, Vol. 32, No. 3, 2016, pp. 560–573.

[33] Schmid, M. and Sattelmayer, T., *Interaction of Acoustic Pressure Fluctuations with Supercritical Nitrogen Jets*.

A. Appendix

A.1. Mean Flame Images

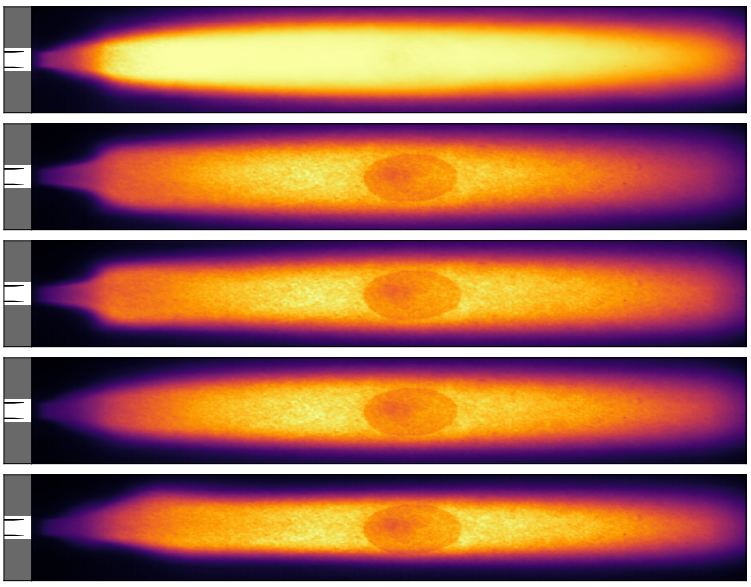

Figure 36.

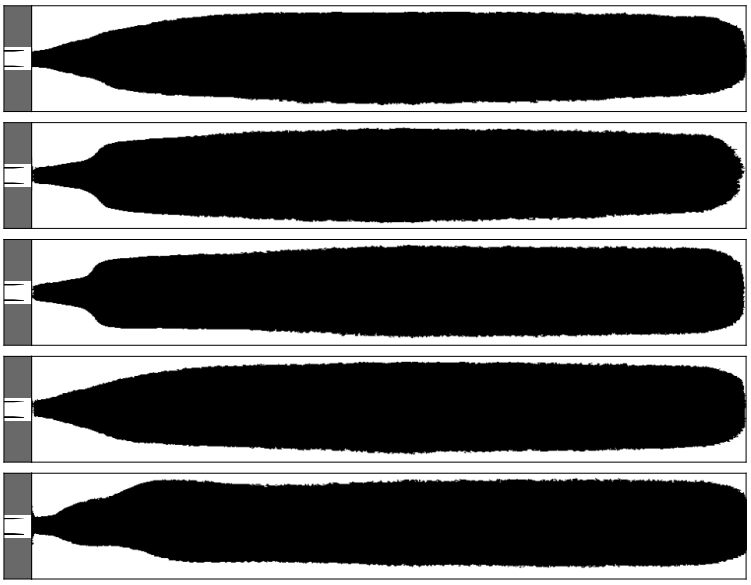

Figure 37.: Binarised time averaged framse

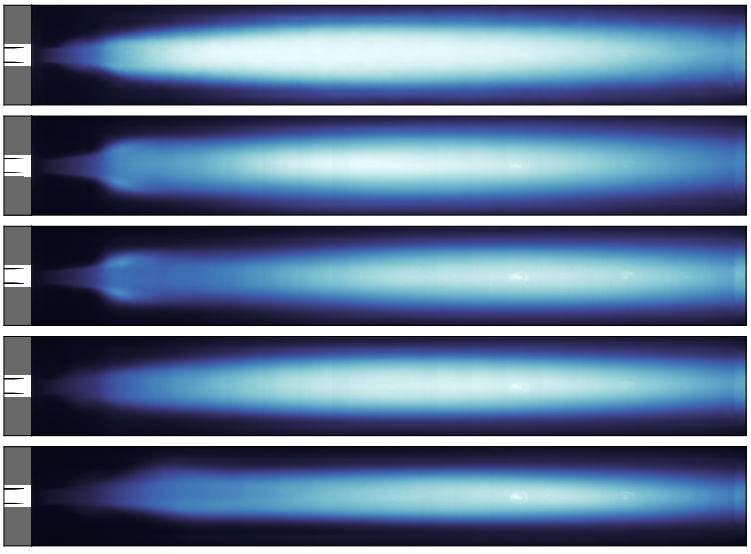

Figure 38.

A.2. OH* and Blue Comparion

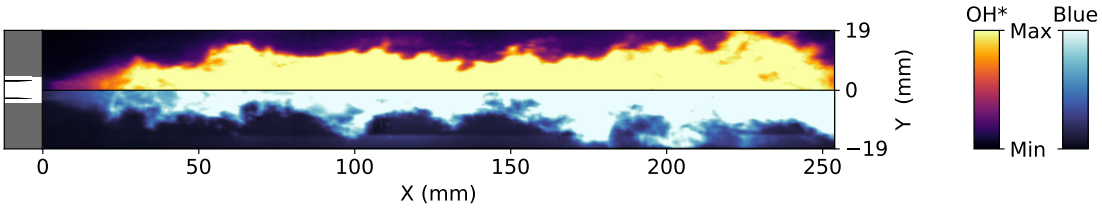

(a) Instantaneous OH* and Blue image

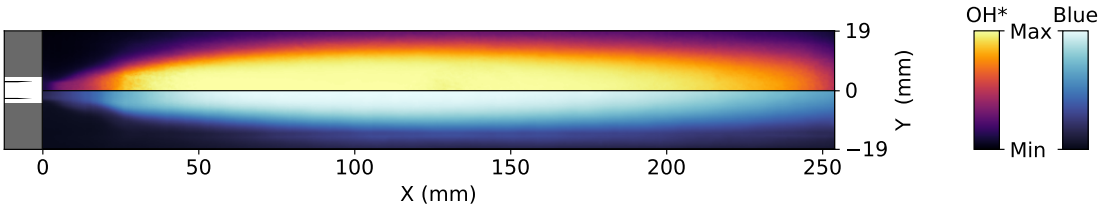

(b) Time averaged OH* and Blue image

Figure 39.: Comparison of OH* and Blue imagery at LP 4

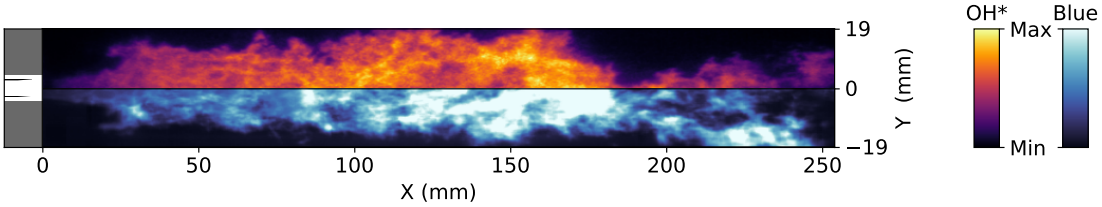

(a) Instantaneous OH* and Blue image

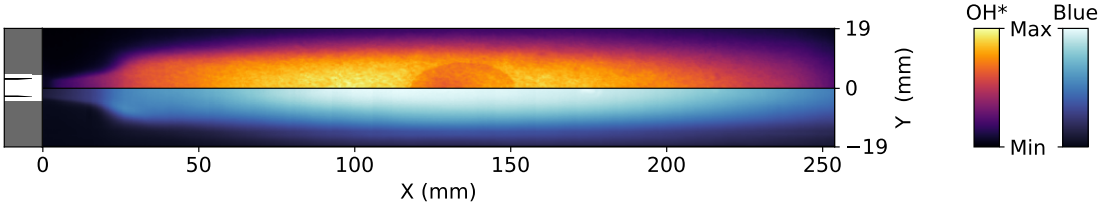

(b) Time averaged OH* and Blue image

Figure 40.: Comparison of OH* and Blue imagery at LP 2

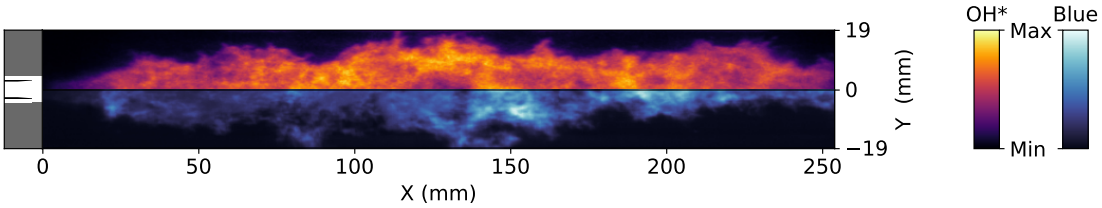

(a) Instantaneous OH* and Blue image

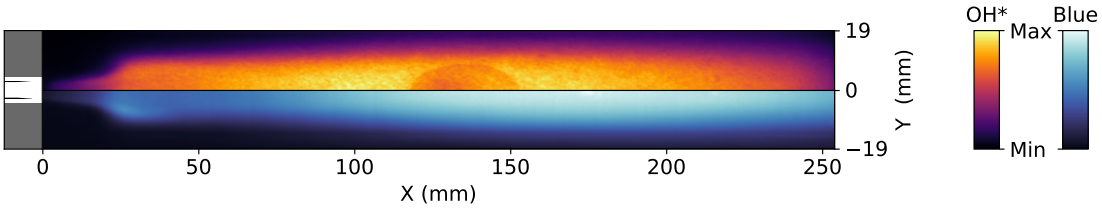

(b) Time averaged OH* and Blue image

Figure 41.: Comparison of OH* and Blue imagery at LP 3

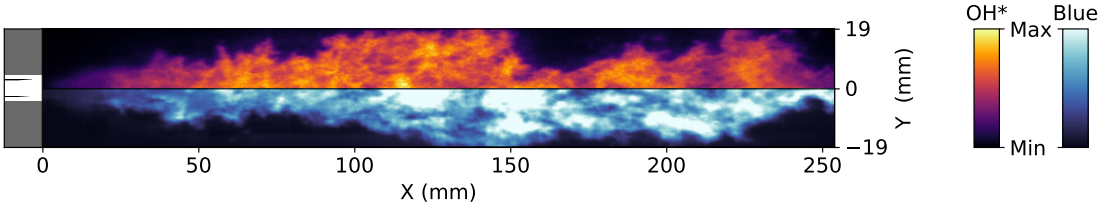

(a) Instantaneous OH* and Blue image

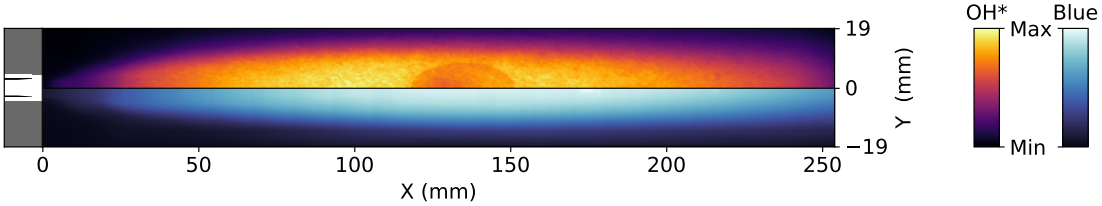

(b) Time averaged OH* and Blue image

Figure 42.: Comparison of OH* and Blue imagery at LP 4

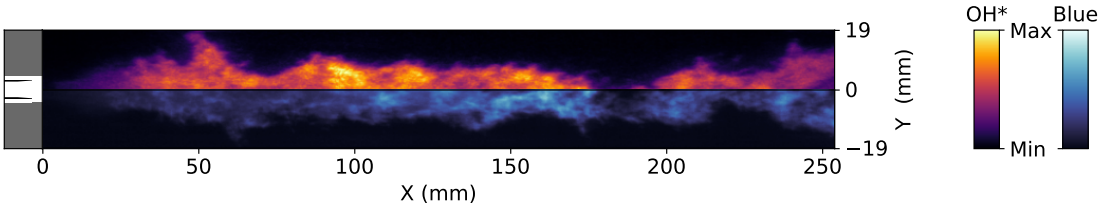

(a) Instantaneous OH* and Blue image

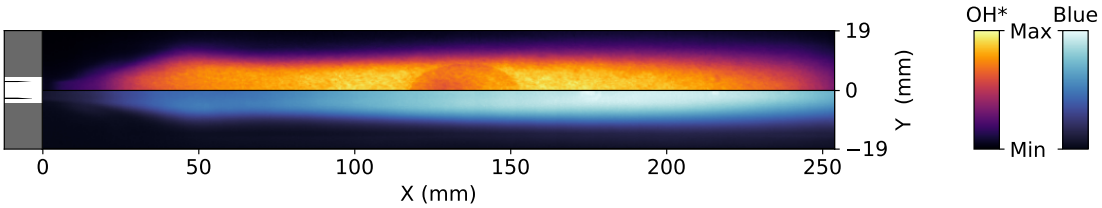

(b) Time averaged OH* and Blue image

Figure 43.: Comparison of OH* and Blue imagery at LP 5